Boosting BDNF in muscle rescues impaired *in vivo* axonal transport in a mouse model of DI-CMTC peripheral neuropathy

Elena R. Rhymes[1,*], Rebecca L. Simkin[1,*], Sunaina Surana[1,2], Yao Tong[3], David Villarroel-Campos[1], Xiang-Lei Yang[3], Giampietro Schiavo[1,2], James N. Sleigh[1,2,#]

[1] Department of Neuromuscular Diseases and UCL Queen Square Motor Neuron Disease Centre, Queen Square Institute of Neurology, University College London, London, UK
[2] UK Dementia Research Institute, University College London, London, UK
[3] Department of Molecular Medicine, The Scripps Research Institute, La Jolla, California, United States of America
* Equal contribution
[#] Correspondence – email: j.sleigh@ucl.ac.uk; telephone: +44(0)20 3108 2722

Abstract

Charcot-Marie-Tooth disease (CMT) is a form of genetic peripheral neuropathy caused by mutations in many functionally diverse genes. The aminoacyl-tRNA synthetase (ARS) enzymes, which charge amino acids to partner tRNAs for protein synthesis, represent the largest protein family linked to CMT aetiology, suggestive of pathomechanistic commonalities. Dominant intermediate CMT type C (DI-CMTC) is caused by *YARS1* mutations driving a toxic gain-of-function in the encoded tyrosyl-tRNA synthetase (TyrRS), which is mediated by exposure of consensus neomorphic surfaces through conformational changes of the mutant protein. In this study, we first showed that DI-CMTC-causing TyrRS^{E196K} mis-interacts with the extracellular domain of the BDNF receptor TrkB, an aberrant association we have previously characterised for CMT type 2D (CMT2D)-causing mutant glycyl-tRNA synthetase. We then performed temporal neuromuscular assessments of recently generated *Yars*^{E196K} mice modelling DI-CMT. Through *in vivo* imaging of exposed sciatic nerves, we determined that *Yars*^{E196K} homozygotes display a selective, age-dependent impairment in axonal transport of neurotrophin-containing signalling endosomes, phenocopying CMT2D mice. Increasing BDNF in DI-CMTC mouse muscle, through injection of recombinant protein or muscle-specific gene therapy, resulted in complete axonal transport correction. Therefore, this work identifies a pathomechanism common to neuropathies caused by mutations in *YARS1* and *GARS1*, and highlights the potential of boosting BDNF in muscles as a therapeutic strategy to treat ARS-related CMTs.

Keywords: aminoacyl-tRNA synthetase (ARS), Charcot-Marie-Tooth disease (CMT), *GARS1*, intravital imaging, motor neuron, neuromuscular junction (NMJ), neurotrophic factors, neurotrophin signalling, peripheral neuropathy, signalling endosome, Trk receptors, *YARS1*.

Introduction

Charcot-Marie-Tooth disease (CMT) is a heritable, genetically diverse form of motor and sensory neuropathy that affects 1 in ≈2,500 people (1, 2). Patients display slowly progressive muscle weakness, muscle wasting and sensory dysfunction, which usually manifests in the hands and feet during adolescence, resulting in life-long disability and a significant health and financial burden on society (3). CMT can be categorised into two principal subtypes depending on pathogenesis and clinical assessment of upper limb motor nerve conduction velocity (NCV) in the median or ulnar nerve: demyelinating/type 1 CMT (CMT1) and axonal/type 2 CMT (CMT2). CMT1 is caused by loss of the myelinating Schwann cells that ensheath peripheral nerves leading to reduced NCV (<38 m/s), whereas CMT2 is caused by loss of peripheral axons and has little effect on NCV (>45 m/s) (4). Some forms of genetic peripheral neuropathy display clinical features of CMT1 and CMT2, including intermediate NCVs (25-45 m/s), and are thus categorised as intermediate CMT (2), although this classification is not always definitive (5).

Mutations in more than 100 genes are currently known to cause CMT and similar purely motor or sensory inherited neuropathies (6). These genes encode proteins integral to a diversity of cellular/neuronal processes, including mitochondrial biogenesis, axonal transport, protein synthesis and endosomal sorting (7). Many forms of CMT1 are caused by mutations in Schwann cell-critical proteins (e.g., peripheral myelin protein 22 and myelin protein zero), which provides a clear rationale for the selective neuropathology characteristic of CMT; however, the pathomechanisms driving motor and sensory dysfunction in CMT2 are less understood, in part, because the causative genes express proteins required by many different cells and tissues. Indeed, the gene family linked to the most CMT subtypes encode aminoacyl-tRNA synthetase (ARS) enzymes, which charge specific amino acids to cognate tRNAs, and are therefore critical to protein synthesis (8).

Seven ARS genes have so far been linked to CMT (*AARS1*, *GARS1*, *HARS1*, *MARS1*, *SARS1*, *WARS1* and *YARS1*) with varying degrees of certainty about pathogenicity (9-15). ARS-related CMTs are all dominantly inherited and display a similar clinical phenotype. Although many ARS mutations affect tRNA aminoacylation, this is not a pre-requisite for disease (8, 16, 17). Rather, a toxic gain-of-function appears to be the primary driver of neuropathology, at least in the well-studied *GARS1*-linked CMT type 2D (CMT2D) (18-22). Indeed, point mutations in *GARS1* have been shown to cause a conformational opening of the encoded mutant glycyl-tRNA synthetase (GlyRS), exposing consensus regions to the protein exterior (23-25). These neomorphic surfaces enable aberrant protein-protein interactions with several different intra- and extra-cellular binding partners, including neuropilin-1 (23), neurotrophin/Trk receptors (26), HDAC6 (27), and G3BP1

(28). Moreover, mutant GlyRS exhibits altered $tRNA^{Gly}$ binding and release, hindering dissociation and causing protein synthesis defects linked to activation of the integrated stress response (ISR) (29, 30).

Heterozygous point mutations in tyrosyl-tRNA synthetase (TyrRS)-encoding *YARS1* cause demyelinating and axonal neuropathy symptoms resulting in a diagnosis of dominant intermediate CMT type C (DI-CMTC) (10). Patients display mild to moderate disease severity with intermediate NCVs and predominant motor versus sensory involvement, which tends to be milder in females (31). DI-CMTC is unlikely to result from haploinsufficiency, since a 50% reduction in *Yars* mRNA produces no overt phenotype in mice (32). Additionally, children with severe, multi-system syndromes caused by biallelic *YARS1* loss-of-function mutations display no clear peripheral neuropathy (33, 34), arguing against a loss of *YARS1* function causing DI-CMTC.

Similar to GlyRS, several different CMT mutations in *YARS1* have been shown to cause mutant TyrRS to adopt an alternative stable conformation (35), which enhances its binding affinity for the transcriptional regulators TRIM28 and HDAC1 (36), as well as F-actin (37). Moreover, a *Drosophila* melanogaster model of DI-CMTC, in which mutant *YARS1* is overexpressed, displays a similar pattern of neuropathology and mRNA translation impairment in motor and sensory neurons to that caused by mutant *GARS1* (20, 38). Furthermore, a new mouse model of DI-CMTC, which carries the E196K mutation in the catalytic domain of TyrRS (*Yars*^{E196K}; see below), displays an activation of the ISR in α motor neurons similar to that identified in CMT2D mice, albeit to a lesser extent (29). It therefore appears that *GARS1*- and *YARS1*-related neuropathies share several key features, suggesting that a common gain-of-function mechanism(s) may mediate neuropathology linked to mutations in the ARS-encoding genes.

To better understand DI-CMTC and provide the first mammalian model of the disease, the Burgess Laboratory engineered the Glu196Lys (c.586G>A; p.E196K) patient mutation into exon 5 of the mouse *Yars* gene (also c.586G>A), creating the *Yars*^{E196K} mouse (29). The $TyrRS^{E196K}$ mutation has little effect on tyrosine aminoacylation (10, 38, 39), hence *Yars*^{E196K} mice can be studied as heterozygotes or homozygotes, unlike mouse models for CMT2D (22, 40, 41). On a C57BL/6N background, heterozygous *Yars*$^{E196K/+}$ mice displayed little to no neuromuscular phenotype. However, homozygous *Yars*$^{E196K/E196K}$ mice have impaired motor performance in the wire hang test, manifesting at 2 months of age and getting marginally worse by 4 and 7 months (32). Additionally, the *Yars*$^{E196K/E196K}$ mutants displayed impaired NCVs by 4 months, as well as reduced calibres of motor, but not sensory, axons without change in axon number or defects in myelination up to 7 months. Whilst the homozygous mutant mice do not precisely model the human genetics of DI-CMTC, they provide an excellent opportunity to assess whether additional phenotypes are shared between DI-CMTC and CMT2D mice, which would be expected if these forms of CMT share underlying pathomechanisms.

In this study, we therefore set out with two main aims: 1) to determine whether the E196K mutation in *YARS1* enables a similar pathological association with the extracellular domain (ECD) of TrkB as that found in CMT2D-linked *GARS1* mutants (26, 42); and 2) to provide a detailed temporal characterisation of neuromuscular phenotypes in *Yars*$^{E196K/+}$ and *Yars*$^{E196K/E196K}$ mice in order to evaluate the neuropathological similarities between ARS-linked neuropathies in a mammalian setting.

Materials and Methods

Animals

Experiments involving mice were performed under license from the UK Home Office in accordance with the Animals (Scientific Procedures) Act (1986) and were approved by the UCL Queen Square Institute of Neurology Ethical Review Committee. Mice were maintained under a 12 h light/dark cycle at a constant room temperature of ≈21˚C with *ad libitum* water and food (Teklad global 18% protein rodent diet, Envigo, 2018C). Cages were enriched with nesting material, plastic/cardboard tubes and wooden chew sticks as standard, and occasionally with cardboard houses. *Yars*^{E196K} mice originally on a C57BL/6N background (provided by Robert W. Burgess, The Jackson Laboratory, Bar Harbor, ME) were backcrossed five times onto the C57BL/6J background and subsequently maintained as heterozygous × wild-type/heterozygous/homozygous breeding pairs. Both males and females were used in experiments, details of which are provided in **Table S1**. To reduce the number of animals used in this study, multiple assessments were performed on individual mice when possible; for instance, a single mouse were used for body weight and grip strength testing, prior to euthanising for dissection of muscles and sciatic nerves. Accordingly, a total of 141 mice was used across all experiments. Animals sacrificed for 3 and 9 month timepoints were 86-99 and 265-287 days old, respectively (see **Table S1**). 8 month-old adeno-associated virus (AAV)-injected *Yars*$^{E196K/E196K}$ mice were aged 243-245 days. Post-natal day 1 (P1) was defined as the day after a litter was first found.

Genotyping

DNA was extracted from ear clips as described previously (43) and the following primers were used in a single PCR for genotyping: Yars_F 5'-TGG CTC CAC CCT ATG AGA AC-3', $Yars^{WT}$_R 5'-AAA CCA CAC CAA CAG CCT TC-3' and $Yars^{E196K}$_R 5'-CCG CGT TAC TTC CTT TTC C-3'. PCR cycling conditions were as follows: 94˚C for 3 min, 35 × [94˚C for 30 s, 60˚C for 35 s, 72˚C for 1 min], 72˚C for 7 min. The wild-type (WT) and E196K sequences produce bands of 598 and 660 bp, respectively.

In vitro pull-down assay

Co-immunoprecipitation experiments using the ECD of human TrkB-Fc (Cys32-His430; R&D Systems, 688-TK) and control human IgG-Fc (110-HG, R&D Systems) were performed in NSC-34 cells (CELLutions Biosystems, CLU140) transfected with plasmids encoding human $TyrRS^{WT}$-V5, $TyrRS^{E196K}$-V5 and $GlyRS^{\Delta ETAQ}$-V5, as previously described (26, 44).

Protein extraction and western blotting

Sciatic nerves and tibialis anterior muscles were dissected from PBS-perfused and non-perfused mice. Proteins were extracted from NSC-34 cells and tissues, and evaluated by western blotting as detailed previously (42). Primary and secondary antibodies used for western blotting are detailed in **Table S2** and **Table S3**, respectively. Densitometry was performed as previously described (43) using total protein stained with 0.1% Coomassie Brilliant Blue R-250 (Thermo Fisher, 20278) as the loading control (45). Hook1 bands at ≈110 kDa and ≈90 kDa were quantified together in sciatic nerves analyses.

Immunofluorescent analyses of DRG and NMJs
Dorsal root ganglia (DRG) from lumbar 1 (L1) to L5 spinal levels were dissected (46), sectioned, stained and analysed as described elsewhere (26). An average of 2,022 ± 96 cells (range 1,428-2,684) across three DRG were assessed in each mouse. The percentages of NF200$^+$ and peripherin$^+$ cells per mouse were calculated by averaging values from the three DRG. Epitrochleoanconeous (ETA), flexor digitorum brevis (FDB) and hind/forelimb lumbrical muscles were dissected, processed for imaging neuromuscular junctions (NMJs), and analysed as detailed previously (47-49). One hundred NMJs per mouse were analysed for assessment of degenerative and maturation phenotypes. Primary and secondary antibodies used for immunofluorescent imaging are detailed in **Table S2** and **Table S3**, respectively. In addition, AlexaFluor555 α-bungarotoxin (α-BTX, Life Technologies, B35451) was used at 1:1,000 to identify post-synaptic acetylcholine receptors (AChRs).

***In vivo* imaging of signalling endosome axonal transport**
Live imaging of signalling endosome axonal transport was performed using an atoxic binding fragment of the tetanus neurotoxin (H_CT, residues 875-1315 fused to a cysteine-rich tag and a human influenza haemagglutinin epitope) produced and labelled as formerly described (50, 51). *In vivo* imaging and analysis of axonal transport was performed as described previously (42, 52, 53). For phenotyping at 3 and 9 months, H_CT was injected under isoflurane-induced anaesthesia into the tibialis anterior on one side of the body and the contralateral gastrocnemius; this enabled transport assessment in peripheral nerves supplying distinct hindlimb muscles of the same mouse. The side of injection was alternated between mice to eliminate time under anaesthesia and right/left biases. Imaging was performed 4-8 h later in both sciatic nerves. By selecting thicker H_CT-positive axons, transport evaluation in motor axons was prioritised (54). To assess trafficking dynamics, 15 endosomes per axon and three axons per mouse were manually tracked using the TrackMate plugin on ImageJ (http://rsb.info.nih.gov/ij/) (55). Endosome frame-to-frame speeds are presented in frequency histograms; a mean of 372 ± 5 movements (range 279-519) per animal were assessed (in a total of 97 mice across the study).

Body weight and grip strength testing
Animals were weighed, and all-limb grip strength was assessed using a Grip Strength Meter (Bioseb, GS3). Mice were assessed on two separate days, on which three trials (separated by at least 5 min) were performed. The maximum recorded values from each of the two days were used to calculate a mean grip strength for each animal. Relative body weight and grip strength were determined by generating the mean value for wild-type mice of each sex and then calculating individual mouse values as a percentage of the wild-type mean of their respective sex.

AAV8-tMCK virus production
Self-complementary AAV (scAAV) expression plasmids were created by OXGENE (Oxford, UK); the incorporated sequences of the 745 bp tMCK promoter, 714 bp eGFP and 744 bp human pre-proBDNF are provided elsewhere (42). pSF-scAAV-tMCK-eGFP and pSF-scAAV-tMCK-BDNF plasmids were packaged into AAV serotype 8 particles by Charles River Laboratories (previously Vigene Biosciences). Viruses were stored at -80˚C in 0.01% (v/v) pluronic F68 surfactant in PBS and diluted in sterile PBS for injection.

Intramuscular injections of BDNF and AAV
To assess the impact of boosting muscle BDNF on endosome axonal transport, bilateral injections into the tibialis anterior muscles of *Yars*$^{E196K/E196K}$ mice were performed under isoflurane-induced anaesthesia. Acute treatment was evaluated in 9 month-old mice by pre-mixing and co-administering 5 µg H_CT-555 with 25 ng recombinant human BDNF (Peprotech, 450-02) into one tibialis anterior muscle and 5 µg H_CT-555 with PBS vehicle into the contralateral tibialis anterior, both in a volume of ≈2.5 µl per muscle. The side of injection was alternated between mice to avoid biases. For analysing longer term treatment, 10 µl bilateral injections of 2.0 × 1011 vg AAV8-tMCK-eGFP into one tibialis anterior and 2.0 × 1011 vg AAV8-tMCK-BDNF into the contralateral tibialis anterior were performed in 8 month-old mice. The side of injection was alternated between mice. 29-30 days post-AAV treatment, *in vivo* axonal transport of signalling endosomes was assessed at 9 months as described above.

Statistics
Data were assumed to be normally distributed unless evidence to the contrary were provided by the Kolmogorov-Smirnov test for normality, while equal variance between groups was assumed. The Bonferroni correction was applied when multiple Kolmogorov-Smirnov tests were performed. Normally-distributed data were statistically analysed using unpaired and paired *t*-tests or one-way and two-way analysis of variance (ANOVA) tests followed by Šídák's multiple comparisons test. Non-normally distributed data were analysed using a Wilcoxon matched-pairs signed rank test or Kruskal-Wallis test followed by Dunn's multiple comparisons test. Sample sizes, which were pre-determined using power calculations and previous experience (26, 42, 47, 48, 54, 56, 57), are reported in figure legends and represent biological replicates (i.e., individual animals). Means ± SEM are plotted for all graphs. All tests were two-sided and an α-level of $P < 0.05$ was used to determine significance. GraphPad Prism 9 software (version 9.5.1) was used for statistical analyses and figure production.

Results

TyrRS^{E196K} mis-interacts with the extracellular domain of TrkB
Neurotrophins are a family of secreted trophic factors that preferentially bind to neuronally-expressed Trk receptors (NGF to TrkA, BDNF and NT/4 to TrkB and NT-3 to TrkC), enabling local and long-range signalling critical to nerve cell homeostasis (58). We have demonstrated that several different forms of human mutant GlyRS aberrantly associate with the ECDs of the neurotrophin receptors, whereas GlyRS^{WT} does not (26, 42). Further, we recently determined that mis-interaction between mutant GlyRS and TrkB, in particular, perturbs axonal transport of neurotrophin-containing signalling endosomes *in vivo*, and that treatment of CMT2D muscles with the TrkB ligand BDNF is able to fully rescue the transport disruption (42). GlyRS is secreted from many different cell types, including neurons and muscle cells, and circulates freely in healthy mouse and human serum (19, 23, 59, 60), underpinning the significance of this mis-interaction *in vivo*.

Our initial aim in this study was therefore to test whether the TyrRS^{E196K} mutant also aberrantly interacts with the ECD of TrkB.

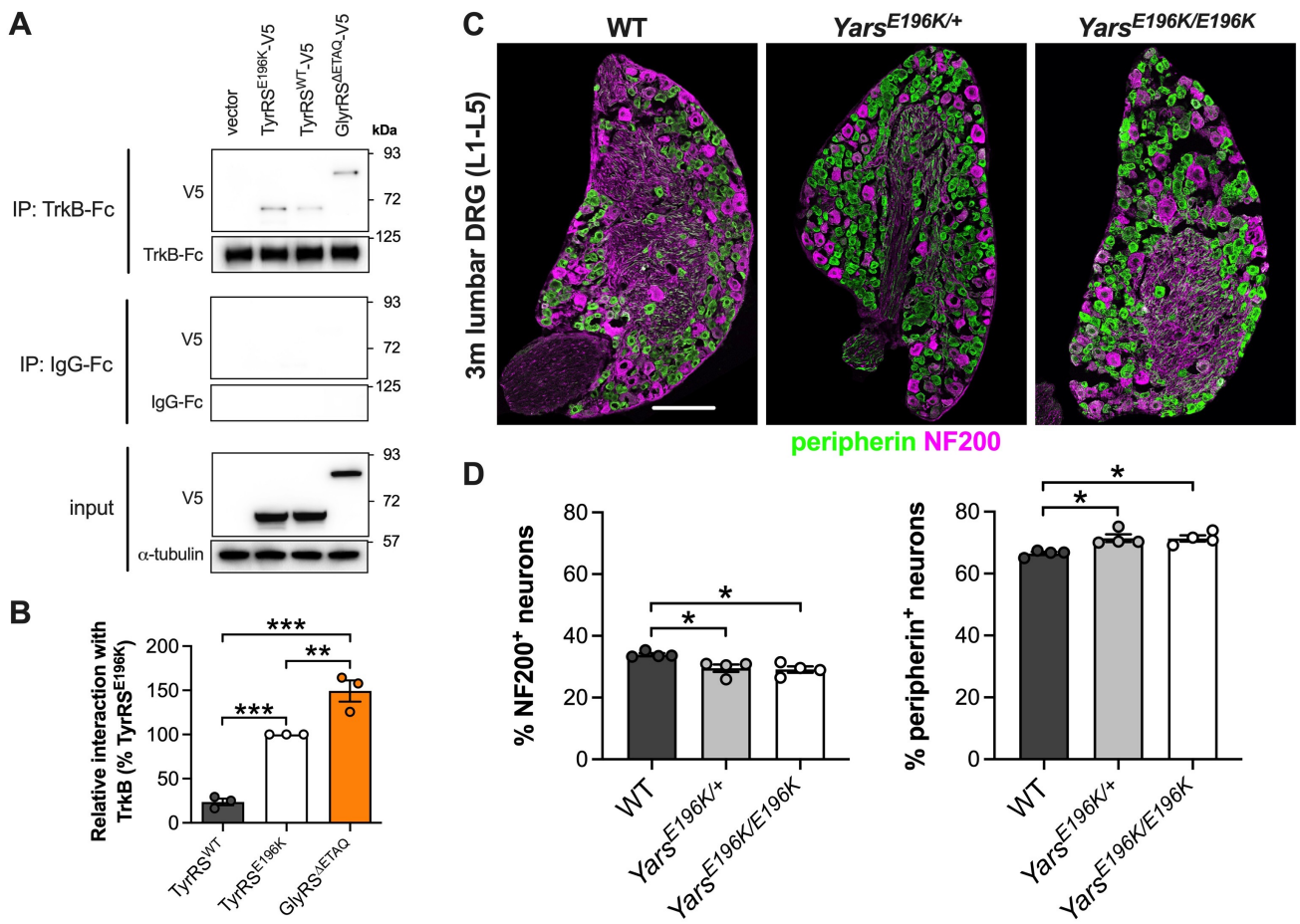

Figure 1. TyrRS^{E196K} aberrantly interacts with the extracellular domain of TrkB and *Yars^{E196K}* mice display altered proportions of sensory neuron subtypes. (**A**) Representative western blots from *in vitro* pull-downs in NSC-34 cells showing that human TyrRS^{E196K} interacts with the extracellular domain of human TrkB-Fc to a greater extent than TyrRS^{WT}. GlyRS$^{\Delta ETAQ}$ was used as a positive control. IP, immunoprecipitation. (**B**) Quantification of the relative interactions between TyrRS^{WT}, TyrRS^{E196K} and GlyRS$^{\Delta ETAQ}$ with TrkB-Fc ($P < 0.001$ one-way ANOVA). $n = 3$. (**C**) Representative immunofluorescent images of 3 month-old wild-type, *Yars$^{E196K/+}$* and *Yars$^{E196K/E196K}$* lumbar DRG sections (10 µm) stained for NF200 (magenta) and peripherin (green). Scale bar = 100 µm. (**D**) *Yars$^{E196K/+}$* and *Yars$^{E196K/E196K}$* mice display a lower percentage of NF200$^+$ neurons (left graph, $P = 0.013$ Kruskal-Wallis test) and a higher percentage of peripherin$^+$ neurons (right graph, $P = 0.013$ Kruskal-Wallis test) in lumbar 1 (L1) to L5 DRG compared to wild-type. $n = 4$. For all graphs, *$P < 0.05$, **$P < 0.01$, ***$P < 0.001$ Šidák's/Dunn's multiple comparisons test; means ± standard error of the mean (SEM) plotted.

To do this, we transfected NSC-34 cells with constructs encoding V5-tagged human TyrRS^{WT}, TyrRS^{E196K} or GlyRS$^{\Delta ETAQ}$, with the latter included as a positive control (42). Cells were subsequently lysed and co-immunoprecipitation experiments performed with the ECD of Fc-tagged TrkB (**Figure 1A**). Western blotting of pull-downs performed in triplicate revealed that TyrRS^{E196K} does indeed mis-associate with TrkB to a higher extent that TyrRS^{WT}, but less than GlyRS$^{\Delta ETAQ}$ (**Figure 1B**). Importantly for a potential shared pathomechanism with GlyRS, TyrRS is also secreted *in vitro* and *in vivo* and is present in serum (61-63).

Yars^{E196K} mice display a perturbation in sensory neuron identity

We have previously revealed that lumbar, but not cervical DRG, of CMT2D mice display fewer NF200$^+$ mechanoreceptors/ proprioceptors and a concomitant increase in the percentage of peripherin$^+$ nociceptors (26, 56). During pre-natal development, sensory neurons can express multiple Trk receptors, reaching their mature Trk identity and function after birth (64). The neuropathic phenotype is thus perhaps linked to the aberrant interaction between mutant GlyRS and the Trk receptors causing a subversion of the differentiation of sensory neuron subclasses.

Given that mutant TyrRS mis-associates with TrkB, we wanted to determine whether *Yars^{E196K}* mice display a similar alteration in sensory neuron populations. We therefore dissected L1-L5 DRG from 3 month-old wild-type, *Yars$^{E196K/+}$* and *Yars$^{E196K/E196K}$* mice and performed immunohistochemical analysis of NF200 and peripherin (**Figure 1C**). Compared to wild-type littermate controls, we identified that both *Yars$^{E196K/+}$* and *Yars$^{E196K/E196K}$* mice display a lower percentage of NF200$^+$ neurons and an increase in the percentage of peripherin$^+$ neurons (**Figure 1D**). Heterozygous and homozygous mutant *Yars* mice thus equally phenocopy CMT2D mice in the perturbation of sensory neuron identity.

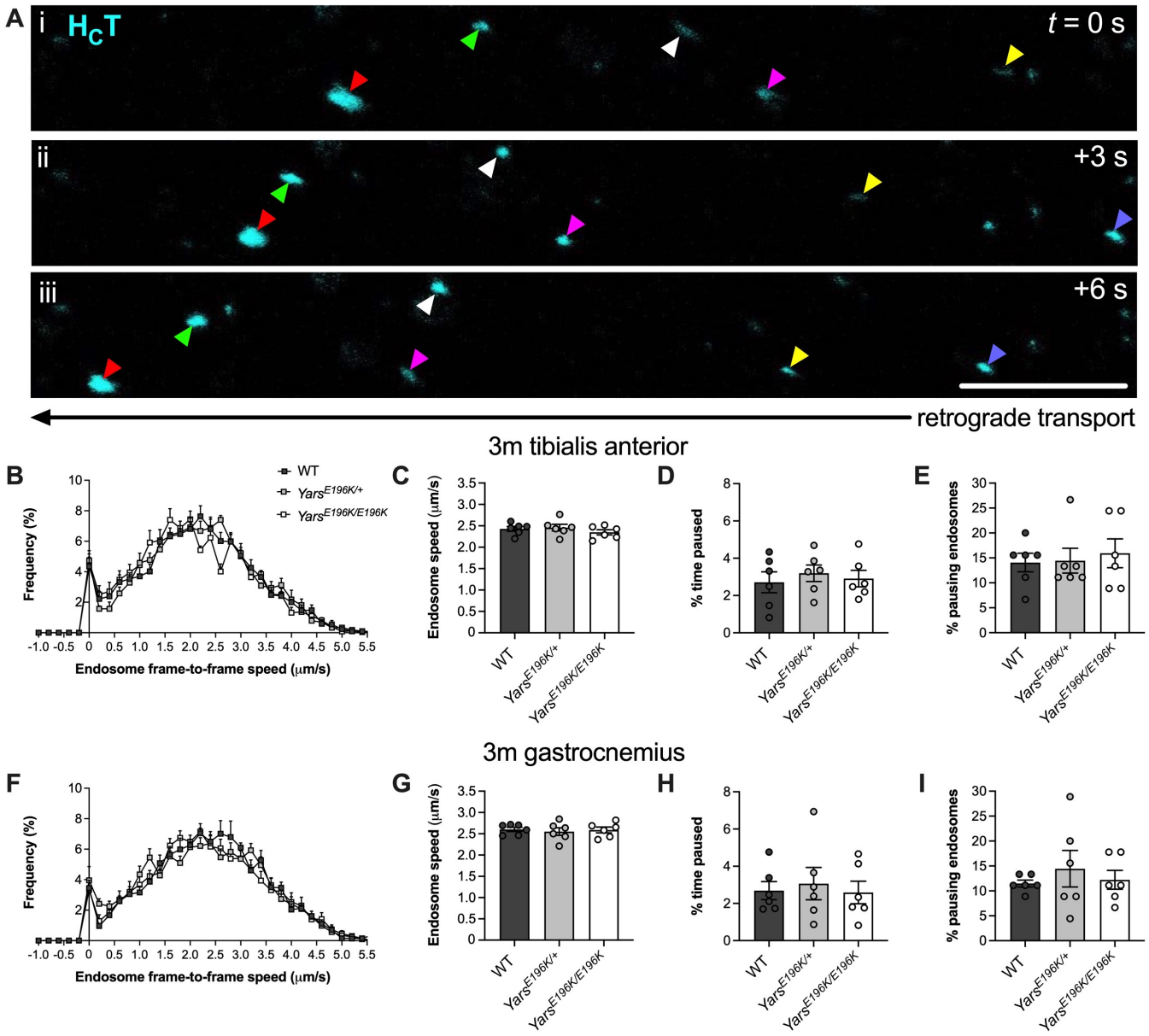

Figure 2. *In vivo* axonal transport of signalling endosomes is unaffected in *Yars*^{E196K} mice at 3 months. (**A**) Representative time-lapse confocal images of signalling endosomes labelled with a fluorescent fragment of tetanus neurotoxin (H_CT, cyan) being retrogradely transported within peripheral nerve axons of live, anaesthetised mice. H_CT-positive endosomes are individually tracked to quantitatively assess their dynamics. Colour-coded arrowheads identify six different endosomes. Scale bar = 10 µm. (**B**) Frame-to-frame speed histogram of signalling endosomes being transported within motor neurons innervating the tibialis anterior muscle of wild-type, *Yars*$^{E196K/+}$ and *Yars*$^{E196K/E196K}$ mice aged 3 months. (**C-E**) There is no difference between genotypes in signalling endosome speed (C, $P = 0.487$), percentage time paused (D, $P = 0.781$) or the percentage of pausing endosomes (E, $P = 0.919$ Kruskal-Wallis test) in neurons innervating the tibialis anterior. (**F**) Frame-to-frame speed histogram of signalling endosomes being transported within motor neurons innervating the gastrocnemius muscle of wild-type, *Yars*$^{E196K/+}$ and *Yars*$^{E196K/E196K}$ mice aged 3 months. (**G-I**) There is no difference between genotypes in signalling endosome speed (G, $P = 0.871$), percentage time paused (H, $P = 0.873$) or the percentage of pausing endosomes (I, $P = 0.671$) in neurons innervating the gastrocnemius. Endosomes within tibialis anterior- and gastrocnemius-innervating axons were analysed in the same mice. For all graphs, genotypes were compared using one-way ANOVAs, unless otherwise stated; $n = 6$; means ± SEM plotted. See also **Figure S7**.

To evaluate the severity of this sensory phenotype compared to the change observed in CMT2D models, the percentage of NF200$^+$ neurons relative to wild-type was calculated for *Yars*$^{E196K/+}$ (87.1 ± 3.5%) and *Yars*$^{E196K/E196K}$ (85.8 ± 3.0%) mice, as well as 3 month-old *Gars*$^{\Delta ETAQ/+}$ mice (73.9 ± 1.4%; data not shown). All DRG assessments were performed by the same researcher (RLS), reducing variability, but relative values were required because the experiments were not performed or analysed in parallel. Statistical comparisons between the three ARS CMT genotypes indicate a difference (*$P = 0.020$ Kruskal-Wallis test),

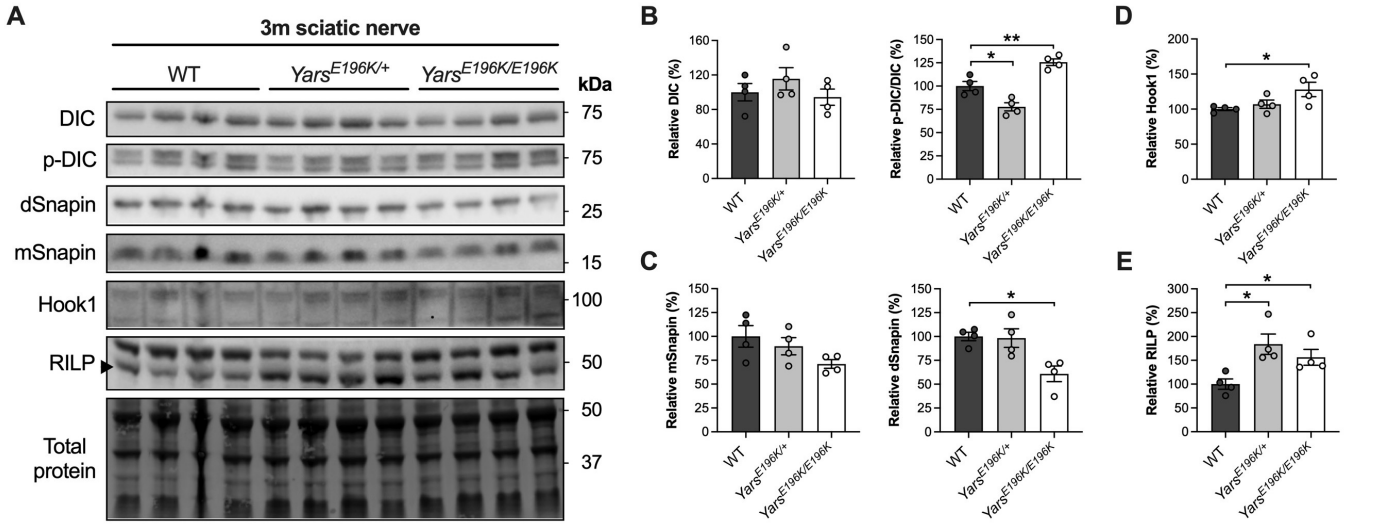

Figure 3. Complementary changes in endosome adaptor levels are observed in sciatic nerves of *Yars*^{E196K} mice at 3 months. (**A**) Western blots of dynein intermediate chain (DIC), phosphorylated DIC (p-DIC) and dynein adaptor proteins Snapin, Hook1 and RILP in sciatic nerves from 3 month-old wild-type, *Yars*$^{E196K/+}$ and *Yars*$^{E196K/E196K}$ mice. (**B-E**) Densitometric analyses of DIC (B, left, $P = 0.399$), p-DIC relative to DIC (B, right, $P < 0.001$), monomeric Snapin (mSnapin, C, left, $P = 0.113$), dimeric Snapin (dSnapin, C, right, $P < 0.01$), Hook1 (D, $P = 0.046$) and RILP (E, $P = 0.018$). The ratio of p-DIC to DIC is reduced in *Yars*$^{E196K/+}$ and increased in *Yars*$^{E196K/E196K}$, the level of dSnapin is reduced in *Yars*$^{E196K/E196K}$ and RILP is increased in both *Yars*^{E196K} genotypes. For all graphs, genotypes were compared using one-way ANOVAs; $n = 4$; *$P < 0.05$, **$P < 0.01$ Šídák's multiple comparisons test; means ± SEM plotted.

and that the reduction in NF200^{+} cells is greater in *Gars*$^{\Delta ETAQ/+}$ lumbar DRG than *Yars*$^{E196K/E196K}$ (*$P = 0.025$ Dunn's multiple comparisons test). Therefore, the disruption in sensory neuron identity correlates with the extent of the mis-interaction between the mutant ARS protein and TrkB.

Body weight, NMJ innervation and grip strength are all unaffected in *Yars*^{E196K} mice at 3 months

The above DRG analyses, and all subsequent experiments, were performed in *Yars*^{E196K} mice on a C57BL/6J background, which was chosen to allow for more appropriate comparisons with the CMT2D strains that are also maintained on C57BL/6J in our laboratory. In the study from the Burgess laboratory, *Yars*^{E196K} mice were assessed at 2, 4 and 7 months and were maintained on the marginally different genetic background of C57BL/6N (32). In the study presented here, we chose to evaluate *Yars*^{E196K} mice at 3 and 9 months to extend the phenotyping age range and allow for assessment of similarities with mutant *Gars* alleles, which we have extensively characterised at 3 months (26, 42, 47, 57).

First, we assessed the body weight of 3 month-old wild-type, *Yars*$^{E196K/+}$ and *Yars*$^{E196K/E196K}$ (**Figure S1**). We observed no differences in body weight or relative body weight of females or males, corroborating previous analyses at 4 and 7 months (32). At 4 months, *Yars*$^{E196K/E196K}$ mice are reported to have reduced NCVs, thinner motor axons and impaired motor function and endurance, as assessed by the wire hang (inverted grid) test (32). We therefore analysed the architecture of NMJs and the maximum grip strength of *Yars*^{E196K} mice. We have previously identified a spectrum of vulnerability to degeneration of NMJs in different muscles in *Gars*$^{C201R/+}$ mice modelling CMT2D (47, 57); at 3 months of age, the ETA muscle in the forearm is almost completely unaffected (≈4% denervation), the hindlimb lumbricals and FDB muscles of the hindpaw display ≈43% and ≈63% denervated NMJs, respectively, and the forelimb lumbricals have an intermediate phenotype with ≈21% denervation. A similar pattern of vulnerability is also observed in *Gars*$^{\Delta ETAQ/+}$ mice at 3 months (data not shown).

These same four muscles were dissected from 3 month-old *Yars*^{E196K} mice and stained to assess NMJ architecture using combined antibodies against SV2/2H3 to identify motor neurons, and fluorescently labelled α-BTX to label post-synaptic AChRs (**Figure S2A**). By assessing the degree of overlap between the pre- and post-synaptic staining and categorising NMJs as either fully innervated, partially denervated or vacant, we can get an understanding of the extent of motor neuron pathology. We observed no NMJ denervation at 3 months of age in *Yars*$^{E196K/+}$ or *Yars*$^{E196K/E196K}$ mice in any of the four muscles (**Figure S2B**). Moreover, the delay in NMJ maturation present in CMT2D mice, assessed by calculating the percentage of NMJs with multiple innervating motor neurons (i.e., polyinnervation) (47, 57), was also absent in *Yars*^{E196K} muscles (**Figure S2C**), with the exception of a small significant difference between forelimb lumbricals of heterozygous and homozygous mutants, which is likely a product of the uniformity in the *Yars*$^{E196K/E196K}$ mouse sample, rather than being biologically meaningful.

Consistent with the lack of morphological disruption at the NMJ, we were unable to detect any difference in females or males between wild-type and *Yars*^{E196K} genotypes in their maximal or relative grip strength (**Figure S3**). This is in contrast to the previously performed wire hang assessments at 2 and 4 months in *Yars*$^{E196K/E196K}$ mice (32), which measure a combination of both muscle function and endurance.

***In vivo* axonal transport of signalling endosomes is unperturbed in *Yars*^{E196K} mice at 3 months**

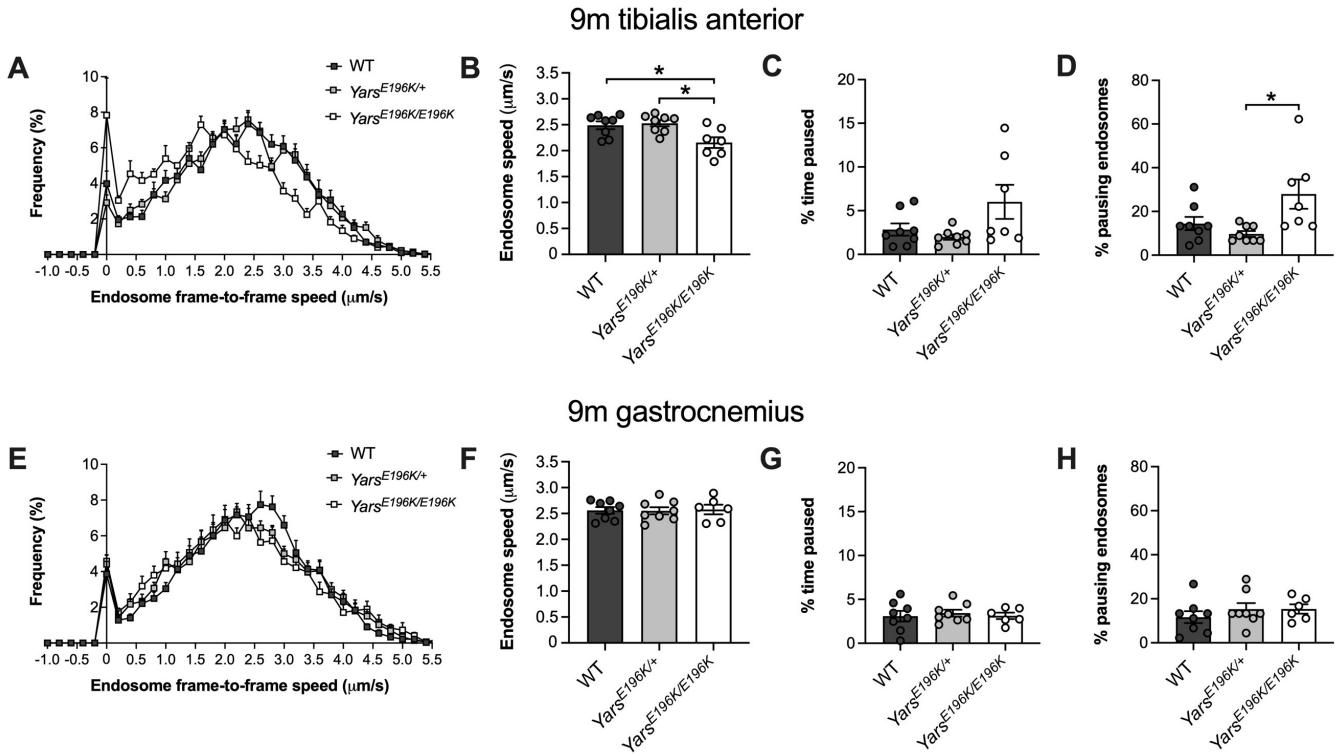

Figure 4. *In vivo* axonal transport is selectively impaired in *Yars*^{E196K} homozygotes at 9 months. (**A**) Frame-to-frame speed histogram of signalling endosomes being transported within motor neurons innervating the tibialis anterior muscle of wild-type, *Yars*$^{E196K/+}$ and *Yars*$^{E196K/E196K}$ mice aged 9 months. (**B**) Signalling endosome speed is reduced in tibialis anterior axons of *Yars*$^{E196K/E196K}$ mice (P = 0.007). (**C-D**) The percentage time paused is unaffected (C, P = 0.053), but the percentage of pausing endosomes is increased (D, P = 0.014) in tibialis anterior axons of *Yars*$^{E196K/E196K}$ mice. (**E**) Frame-to-frame speed histogram of signalling endosomes being transported within motor neurons innervating the gastrocnemius muscle of wild-type, *Yars*$^{E196K/+}$ and *Yars*$^{E196K/E196K}$ mice aged 9 months. (**F-H**) There is no difference between genotypes in signalling endosome speed (F, P = 0.971), percentage time paused (G, P = 0.848) or the percentage of pausing endosomes (H, P = 0.529 Kruskal-Wallis test) in motor neurons innervating the gastrocnemius. Endosomes within tibialis anterior- and gastrocnemius-innervating axons were analysed from the same mice. For all graphs, genotypes were compared using one-way ANOVAs, unless otherwise stated; n = 6-8; *P < 0.05 Šidák's multiple comparisons test; means ± SEM plotted. See also **Figure S7** and **Figure S9**.

Gars$^{C201R/+}$ mice display impaired *in vivo* axonal transport of neurotrophin-containing signalling endosomes at 1 and 3 months of age, which manifests as a reduction in endosome trafficking speed after P15-16 (42). This defect was identified by injecting a fluorescent retrograde probe known as H_CT into the tibialis anterior and gastrocnemius muscles of anaesthetised mice, followed by time-lapse confocal imaging of the exposed sciatic nerve under terminal anaesthesia (52). H_CT binds to and is internalised at the NMJ, prior to being sorted into signalling endosomes for retrograde axonal transport within motor axons (65). Individual endosomes can be subsequently imaged, tracked and their dynamic properties assessed.

We therefore used H_CT to identify whether *Yars*^{E196K} mice display an impairment in endosome axonal transport at 3 months of age (**Figure 2A**). However, rather than injecting both the tibialis anterior and gastrocnemius muscles together, we performed assessments of transport separately in these two muscles, as we have recently determined that their innervating axons can be differentially affected by disease in a mouse model of amyotrophic lateral sclerosis (66). The most common clinical signs reported in a small cohort of familial DI-CMTC patients were weakness and atrophy of the tibialis anterior and gastrocnemius (67), thus these two muscles are clinically relevant for the transport assessments. However, in motor neurons innervating the tibialis anterior muscle, we observed no differences between genotypes in signalling endosome speed (**Figure 2B-C**), the percentage time that endosomes remained stationary (**Figure 2D**) or the percentage of endosomes that paused (**Figure 2E**). A similar situation was observed in gastrocnemius-innervating motor neurons (**Figure 2F-I**). Together, these results indicate that at 3 months of age, *Yars*^{E196K} mice display no disruption in axonal transport of signalling endosomes, commensurate with our body weight, NMJ and grip strength analyses.

We have previously determined that signalling endosome trafficking impairment in CMT2D mice correlates with reduced availability of adaptor proteins critical to endosome transport (42). As we see no transport deficits in the sciatic nerve of *Yars*^{E196K} mice at 3 months, we hypothesised that there would be no corresponding change in the levels of the adaptor proteins Snapin (68), Hook1 (69) or RILP , which have been shown to play a role in signalling endosome transport. We also probed for levels of dynein intermediate chain (DIC), a major component of the retrograde motor protein cytoplasmic dynein (70), as well as for dynein phosphorylation at residue S81 (p-DIC), which facilitates

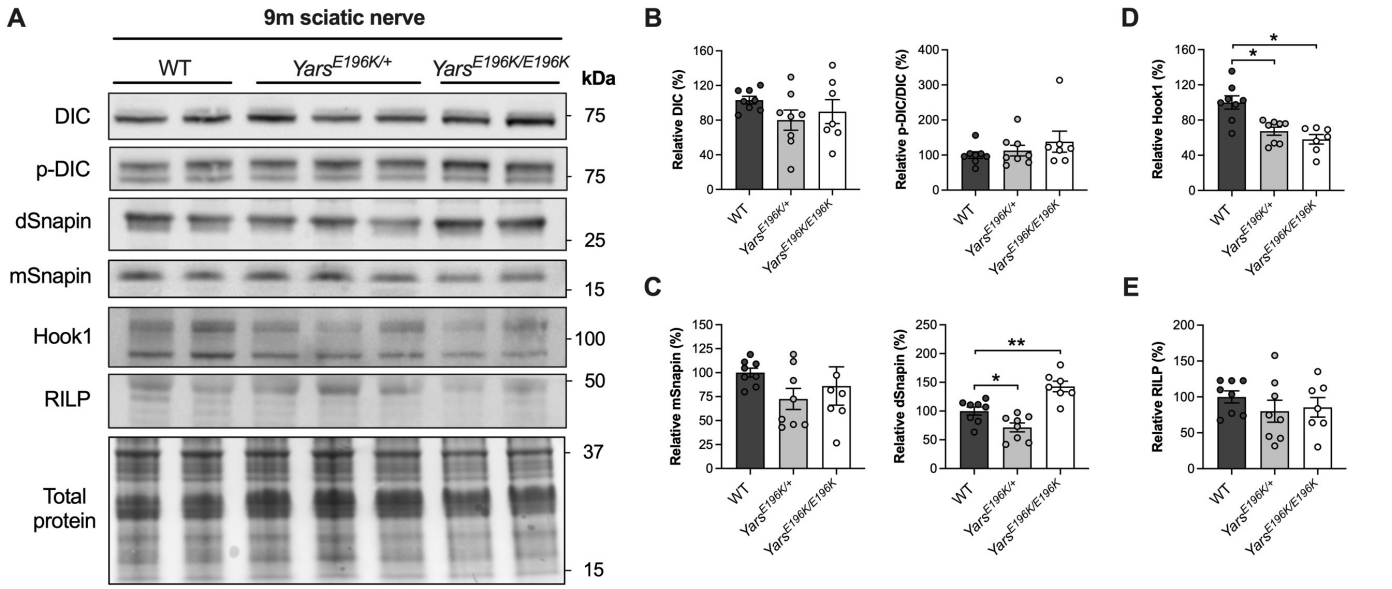

Figure 5. Endosome adaptor levels are altered in 9 month-old *Yars*^{E196K} sciatic nerves. (**A**) Western blots of dynein intermediate chain (DIC), phosphorylated DIC (p-DIC) and dynein adaptor proteins Snapin, Hook1 and RILP in sciatic nerves from 9 month-old wild-type, *Yars*$^{E196K/+}$ and *Yars*$^{E196K/E196K}$ mice. (**B-E**) Densitometric analyses of DIC (B, left, $P = 0.298$), p-DIC relative to DIC (B, right, $P = 0.541$ Kruskal-Wallis test), monomeric Snapin (mSnapin, C, left, $P = 0.320$), dimeric Snapin (dSnapin, C, right, $P < 0.001$), Hook1 (D, $P = 0.003$ Kruskal-Wallis test) and RILP (E, $P = 0.517$). The level of dSnapin is reduced in *Yars*$^{E196K/+}$ and increased in *Yars*$^{E196K/E196K}$, and the level of Hook1 is reduced in both *Yars*^{E196K} genotypes. For all graphs, genotypes were compared using one-way ANOVAs, unless otherwise stated; $n = 7$-8; *$P < 0.05$, **$P < 0.01$ Šídák's/Dunn's multiple comparisons test; means ± SEM plotted.

the selective recruitment of the motor to signalling endosomes for retrograde trafficking upon Trk activation (71). Contrary to expectation, we saw that DIC phosphorylation was reduced in *Yars*$^{E196K/+}$ mice, alongside an increase in RILP levels. In *Yars*$^{E196K/E196K}$ mice, dimeric Snapin (dSnapin) levels were reduced, whereas p-DIC, Hook1 and RILP were all increased (**Figure 3**). Although the cause of these changes is unknown, it is enticing to speculate that there may be compensatory mechanisms in endosome adaptor availability that ensure signalling endosome transport remains unaffected.

Summarising the phenotype of *Yars*^{E196K} mice on a C57BL/6J background at 3 months, we observed a perturbation in sensory neuron identity and changes in adaptor protein levels in the sciatic nerve, but no deficits in body weight, NMJ innervation, maximal grip strength or *in vivo* axonal transport of signalling endosomes.

Yars$^{E196K/E196K}$ mice display marginally reduced body weight, but normal motor innervation and function at 9 months

As we detected only subtle changes in *Yars*^{E196K} mice at 3 months of age, we decided to re-assess mice at 9 months of age, extending beyond the 7 months originally evaluated (32). We observed a small reduction in body weight and relative body weight of 9 month-old *Yars*$^{E196K/E196K}$ females compared to *Yars*$^{E196K/+}$, but not *Yars*^{WT} (**Figure S4A-B**). Males were unaffected, suggesting that there may be a subtle sex-specific defect. When relative body weights of females and males were combined, we also saw a mild deficit in *Yars*$^{E196K/E196K}$ compared to *Yars*$^{E196K/+}$, but again not in comparison to *Yars*^{WT} (**Figure S4C**).

Mirroring the lack of a large reduction in body weight, we observed no degeneration of NMJs across the same four muscles analysed at 3 months (**Figure S5**). Of the six *Yars*$^{E196K/E196K}$ mice analysed, five were female, indicating that there is unlikely to be sex-specific denervation. This is supported by the finding that *Yars*^{E196K} females and males display normal grip strength at 9 months (**Figure S6**).

In vivo endosome axonal transport is defective in *Yars*$^{E196K/E196K}$ mice at 9 months

We next evaluated *in vivo* axonal transport of signalling endosomes in motor axons innervating the tibialis anterior and gastrocnemius muscles of 9 month-old mice. *Yars*$^{E196K/+}$ mice were indistinguishable from *Yars*^{WT} (**Figure 4** and **Figure S7**). However, *Yars*$^{E196K/E196K}$ mice displayed a reduction in endosome trafficking speeds in tibialis anterior-innervating neurons, coupled with an increase in the percentage of pausing endosomes (**Figure 4A-D** and **Figure S7A-B**). This deficit appears to be selective to neurons innervating the tibialis anterior, as we saw no such impairments in gastrocnemius-innervating neurons (**Figure 4E-H** and **Figure S7C**).

We also evaluated endosome adaptor levels in 9 month-old sciatic nerves to determine whether any clear patterns could be linked to the transport disruption. None of the significant changes identified in 3 month-old nerves were replicated in the older mice and fewer changes were observed in homozygous mutants at the later time point compared with the earlier age (**Figure 5**). At 9 months, *Yars*$^{E196K/+}$ mice displayed a reduction in the availability of dSnapin and Hook1, whereas *Yars*$^{E196K/E196K}$ possessed higher levels of dSnapin and lower levels of Hook1 (**Figure 5C-D**).

Augmenting BDNF levels in muscles of *Yars*$^{E196K/E196K}$ mice rescues axonal transport

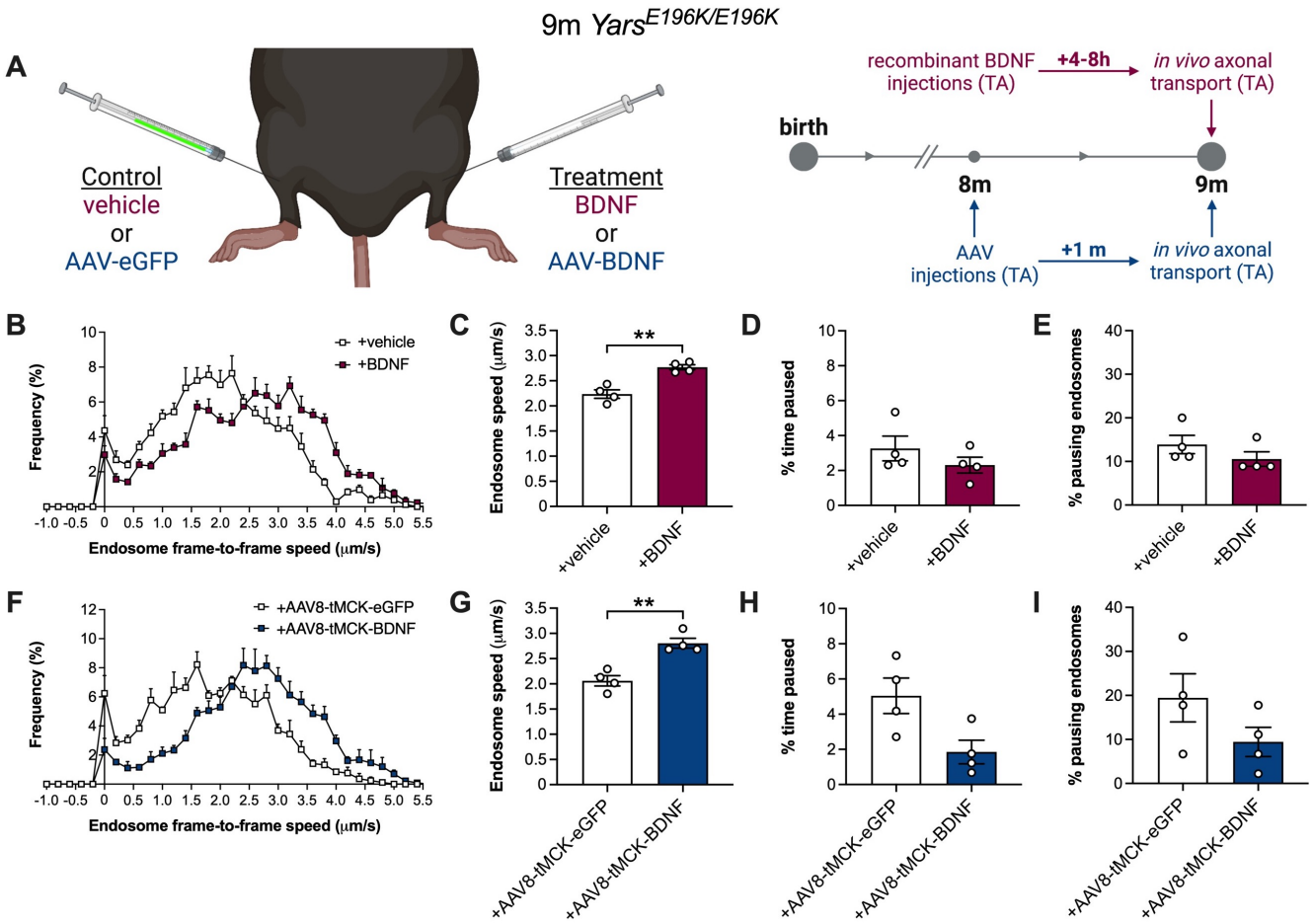

Figure 6. Boosting BDNF in muscles of homozygous *Yars*^{E196K} mice rescues *in vivo* axonal transport of signalling endosomes. (**A**) Schematics depicting the dual-tibialis anterior injection paradigms (left) and timelines (right) used in experiments to assess the impact of BDNF treatment in *Yars*$^{E196K/E196K}$ mice. Animals either received dual injections of vehicle control versus recombinant BDNF at 9 months (maroon, top) or dual injections of AAV8-tMCK-eGFP versus AAV8-tMCK-BDNF at 8 months (blue, bottom). *In vivo* axonal transport of signalling endosomes was evaluated in tibialis anterior (TA)-innervating motor neurons at 9 months. (**B**) Frame-to-frame speed histogram of signalling endosomes being transported within motor neurons innervating the tibialis anterior muscle of 9 month-old *Yars*$^{E196K/E196K}$ mice 4-8 h post-treatment with intramuscular injections of vehicle or 25 ng recombinant BDNF. (**C-E**) BDNF increases the *in vivo* axonal transport speed of signalling endosomes in *Yars*$^{E196K/E196K}$ (C, $^{**}P = 0.004$), without impacting the percentage time paused (D, $P = 0.324$) or the percentage of pausing endosomes (E, $P = 0.625$ Wilcoxon matched-pairs signed rank test). (**F**) Frame-to-frame speed histogram of signalling endosomes being transported within motor neurons innervating the tibialis anterior muscle of 9 month-old *Yars*$^{E196K/E196K}$ mice 29-30 days after bilateral injection of AAV8-tMCK-eGFP into one tibialis anterior and AAV8-tMCK-BDNF into the contralateral tibialis anterior. (**G-I**) AAV8-tMCK-BDNF increases signalling endosome speed in *Yars*$^{E196K/E196K}$ (G, $^{*}P = 0.032$), without impacting the percentage time paused (H, $P = 0.116$) or the percentage of pausing endosomes (I, $P = 0.299$). For all graphs, treatments were compared using paired *t*-tests, unless otherwise stated; $n = 4$; means ± SEM plotted. See also **Figure S8** and **Figure S9**.

As *Yars*$^{E196K/E196K}$ mice display a muscle-selective and age-dependent disruption in transport, similar in nature to that observed in CMT2D mice (42), we wished to establish whether increasing the availability of BDNF could also alleviate the trafficking disruption in this DI-CMTC model. To do so, we harnessed two different strategies – an acute paradigm with recombinant BDNF and a longer-term approach with AAV8-mediated, muscle-selective BDNF expression (**Figure 6A**).

We first evaluated the short-term effect of injecting recombinant human mature BDNF into muscles of 9 month-old *Yars*$^{E196K/E196K}$ mice. This was done by co-injecting PBS vehicle control plus fluorescent H_CT into one tibialis anterior muscle, and BDNF together with H_CT into the contralateral muscle; signalling endosome transport was then sequentially assessed in both sciatic nerves 4-8 h-post injection. BDNF treatment caused an overt increase in the speed of signalling endosomes without significantly affecting pausing (**Figure 6B-E**), indicating that it is capable of rescuing the trafficking deficit. The endosome transport dynamics of vehicle-treated mice were similar to those previously identified in tibialis anterior-innervating axons of 9 month-old *Yars*$^{E196K/E196K}$ mice (average speed: untreated 2.16 ± 0.1 μm/s versus vehicle-treated 2.24 ± 0.1 μm/s, $P = 0.615$ unpaired *t*-test).

The impact of longer-term exposure of *Yars*$^{E196K/E196K}$ muscles to increased BDNF availability was analysed by injecting 8 month-old mice with AAV8-tMCK-eGFP control into one tibialis anterior and AAV8-tMCK-BDNF into the contralateral muscle. We have

previously confirmed that the combination of muscle-tropic AAV serotype 8 (72) with the muscle-specific promoter tMCK (73) drives a robust increase in BDNF expression in muscles up to at least 30 days *in vivo* (42). We therefore adapted this approach and treated 8 month-old *Yars*$^{E196K/E196K}$ mice with bilateral injections of AAV into tibialis anterior muscles, before assessing transport of signalling endosomes at 9 months. We first confirmed that AAV treatment did indeed drive transgene expression in tibialis anterior muscles (**Figure S8**). We then showed that treatment with AAV8-tMCK-BDNF caused a strong increase in signalling endosome transport speed (**Figure 6F-G**), without significantly altering pausing (**Figure 6H-I**). Once again, we confirmed that the control virus had no impact on transport by comparing AAV8-tMCK-eGFP-treated mice with the original tibialis anterior-innervating axon data from 9 month-old *Yars*$^{E196K/E196K}$ mice (average speed: untreated 2.16 ± 0.1 μm/s versus eGFP-treated 2.06 ± 0.1 μm/s, $P = 0.562$ unpaired *t*-test). This indicates that treatment with AAV8-tMCK-BDNF has a local effect within the injected muscle and does not systemically affect transport.

Given the female-specific reduction in *Yars*$^{E196K/E196K}$ body weight (**Figure S4**), we compared transport in tibialis anterior-innervating neurons between 9 month-old *Yars*$^{E196K/E196K}$ females and males, grouping all mice not receiving BDNF treatment (i.e., incorporating PBS vehicle- and AAV8-tMCK-eGFP-treated mice into the original 9 month data set). There was no difference in endosome trafficking between females and males (**Figure S9A-D**), suggesting that sex-specific differences are restricted to body weight and that transport in both sexes is equally defective.

Finally, to better evaluate whether treatment with BDNF is able to impact endosome pausing, we combined control-treated and BDNF-treated data from the acute and long-term transport experiments. Doing so revealed that boosting intramuscular levels of BDNF has a clear rescue effect on the axonal transport disruption in DI-CMTC mice (**Figure S9E-H**) – signalling endosome transport speeds were increased almost to WT levels, and both percentage pause time and the percentage of pausing endosomes were reduced.

Discussion

Disturbances in axonal transport have been identified in models of many different forms of both genetic and acquired peripheral neuropathy (74-76), including cellular and *in vivo* models of CMT2D (27, 42, 77, 78); however, whether these deficits are a primary cause of disease or simply a secondary consequence of neuropathology remains an open question. While we have not determined whether impaired endosome trafficking is a driver of neuropathy in *Yars*^{E196K} mice, we do provide the first evidence for its dysfunction in DI-CMTC and only the second study in which axonal transport has been identified as being impaired in mammalian peripheral neuropathy *in vivo*. Moreover, other than the alteration in sensory neuron populations, the reduced endosome transport speeds and altered endosome adaptor levels are the first and only clear phenotypes we identified in DI-CMTC mice on the C57BL/6J background (**Figure S10**). However, we will have to extend the phenotyping age range beyond 9 months to determine whether additional neuropathic phenotypes, such as loss of NMJ integrity, begin to manifest subsequent to the transport disruption.

For better comparison with our other neuropathic mice, we moved the *Yars*^{E196K} mutation from the C57BL/6N to the C57BL/6J background. This may have inadvertently reduced the overall severity of the DI-CMTC mice. Hines and colleagues report wire hang disruption at 2 months of age in *Yars*^{E196K} homozygotes, followed by reduced NCVs and motor axon calibres by 4 months (32), while we report no disruption in NMJ connectivity across four different muscles, nor a decline in maximal grip strength even at 9 months. It is certainly feasible that the diminished motor axon calibres cause slower NCVs and reduced motor endurance without impacting NMJ innervation and maximum motor force; indeed, reduced NCV occurs without denervation in several mouse models of neuropathy (79-81). Alternatively, we may have missed subtle morphological alterations at the neuromuscular synapse (e.g., reduced post-synaptic area or complexity), NMJ pathology may be present in muscles different to those analysed (e.g., the tibialis anterior), or by calculating the percentage of NMJs displaying degeneration, we could have missed denervated NMJs that have been rapidly lost from the muscle (82).

To determine whether genetic background is the cause for the potential discrepancy between studies, we are currently evaluating whether α motor neurons in the spinal cord of *Yars*^{E196K} mice on the C57BL/6J background display the same activation of the ISR as previously reported (29). If lumbar motor neurons display activation of the ISR, it would indicate that a key feature of neuropathy is indeed present and that the perceived distinction in model severity between studies is simply due to the different analyses performed. However, if the ISR is not activated, it will imply that genetic background influences the effect of the *Yars*^{E196K} mutation, perhaps through subtle alterations in availability of TyrRS, TrkB, or prospective mis-interaction partners such as tRNA^{Tyr}. Genetic background can drastically modify the severity of mutations in mice modelling neurological disease (83), including *Gars*^{P278KY} and *Gars*^{C201R} (40, 41), suggesting that this is the most likely explanation for the limited neuromuscular phenotype we observed. Nevertheless, the lack of axonal transport impairment at 3 months in *Yars*$^{E196K/E196K}$ mice, followed by disturbance at 9 months, suggests that the trafficking disruption is degenerative and progressive, and therefore similar in nature to that identified in CMT2D mice (42).

The relevance of changes in endosome motor adaptor protein levels in 3 and 9 month sciatic nerves of *Yars*^{E196K} mice remains unclear, as we did not see consistent patterns correlating with age and/or the development of axonal transport disruption. A possible explanation for this is that different motor adaptor proteins may be required for signalling endosome trafficking as they progress from distal to proximal segments of the axon (84). Indeed, the retrograde delivery of signalling endosomes is dependent upon acquisition of Rab7 (85), whereas different effectors are critical for the retrograde transport and maturation of autophagosomes (86). Therefore, impairments in BDNF-TrkB signalling at the axon terminal caused by mutant TyrRS interacting with TrkB may have multifarious age- and location-dependent effects on the endosome motor adaptors, obscuring a clear neuropathic signature. That being said, the three endosome adaptors that were increased at 3 months in *Yars*$^{E196K/E196K}$ nerves were no longer elevated at 9

months, perhaps indicative of a possible loss of compensatory mechanisms with age.

We currently do not fully understand the molecular mechanisms underlying the defective axonal transport process in mutant *Yars* mice, but it is likely related to the aberrant association between mutant TyrRS and the ECD of the BDNF receptor TrkB. Mutations in *YARS1* enhance the interaction of TyrRS with natural binding partners TRIM28 and HDAC1 (36), as well as F-actin (37). In this study, $TyrRS^{WT}$ also appears to interact with TrkB at a low level, whereas previous data indicate that this is not the case for $GlyRS^{WT}$ (26, 42). Therefore, it is possible that $TyrRS^{WT}$ interacts with TrkB to exert a non-canonical function, rather than being a novel aberrant association, but further work is required to address this finding. We have previously determined that inhibition of the TrkB-BDNF signalling pathway in WT muscles *in vivo*, either pharmacologically with a pan-Trk inhibitor or using BDNF blocking antibodies, results in impaired signalling endosome trafficking in otherwise healthy motor axons (42). It is thus conceivable that $TyrRS^{E196K}$ from the muscle is mis-interacting with TrkB at motor nerve terminals, impinging upon BDNF signalling and slowing down endosome trafficking. Consistent with this hypothesis, provision of excess BDNF in DI-CMTC muscles fully corrects the transport phenotype. As we do not see deficits in this dynamic process in heterozygous $Yars^{E196K}$ mice, it is likely a dose-dependent disruption, which is consistent with previous reports that $Yars^{E196K}$ heterozygous mice are relatively unaffected compared to homozygotes, and that *Yars* expression in the spinal cord is similar between wild-type, $Yars^{E196K/+}$ and $Yars^{E196K/E196K}$ mice (29, 32). Supporting this idea, the $GARS1^{\Delta ETAQ}$ mutation, which drives a more severe neuropathy phenotype in mice compared to $YARS1^{E196K}$, including early disruption of signalling endosome transport (22, 42), causes mutant GlyRS to bind more strongly than $TyrRS^{E196K}$ to the ECD of TrkB. This interaction between $TyrRS^{E196K}$ and TrkB is likely to impair the ability of BDNF to signal through TrkB, which could result in the slowing of neurotrophin-containing signalling endosomes via several different, non-mutually exclusive mechanisms, including reduced translation and/or recruitment of adaptor and motor proteins (71, 87, 88). We are currently working to understand the molecular mechanism underpinning the slowed transport and have previously discussed these possibilities (42), so will not elaborate further here. It remains unknown why the $TyrRS^{E196K}$ dosage does not differentially affect the sensory neuron populations in lumbar DRG of $Yars^{E196K}$ mice; however, the data suggest that, since this is a toxic gain-of-function, once a maximum threshold level of mutant TyrRS is available (such as that reached in the heterozygous mutants) no further changes to sensory neuron populations occur.

As aminoacyl-tRNA synthetases represent the largest protein family linked to CMT aetiology, it is an alluring prospect that they share a common pathomechanism, which can be targeted to treat the several different associated subtypes of CMTs. Supporting this possibility, mouse and fly models of CMT2D and DI-CMTC display protein synthesis impairments in motor neurons linked to the ISR, which are driven by $tRNA^{Gly}$ sequestration and ribosome stalling in mutant *Gars* models (20, 29, 30). Moreover, shared genetic modifiers of pathology have been discovered in *Drosophila* models of *GARS1*- and *YARS1*-associated neuropathy (89). Our work adds to the possibility of a mutual mechanism between CMT2D and DI-CMTC causing impairment in signalling endosome axonal transport through perturbations of the BDNF-TrkB signalling axis. There is scope for this pathomechanism to be relevant to additional ARS-linked neuropathies, since structural relaxation and conformational opening have been reported for both CMT-linked alanyl-tRNA synthetase (90) and histidyl-tRNA synthetase (91). Mammalian models for other subtypes of ARS-linked neuropathy are currently unavailable to determine whether axonal transport disruption is impaired in a mammalian setting *in vivo*, although with the advent of CRISPR/Cas9 technology, they are likely forthcoming. While the interruption in cargo trafficking within axons may not be the primary cause of neuropathy linked to ARS mutations, it will certainly contribute to the demise of peripheral nerves and is a promising candidate process for pharmacological targeting (92, 93).

Through acute and long-term treatment paradigms, we have shown that boosting the availability of BDNF at motor nerve terminals of $Yars^{E196K/E196K}$ mice rescues deficits in axonal transport of neurotrophin-containing signalling endosomes *in vivo*, replicating findings in CMT2D mice (42). This strategy may therefore provide a broadly effective approach to treating ARS-linked neuropathies, which currently lack any approved clinical therapies. In combination with additional treatments that have proven beneficial in mutant *Gars* mice, including HDAC6 inhibition (27, 77, 78), delivery of neurotrophin 3 (94) and $VEGF_{165}$ (23), and provision of excess $tRNA^{Gly}$ (30), boosting BDNF in muscles may serve as part of a combinatorial treatment to address the therapeutic needs of one of the most common inherited neuromuscular conditions.

Author Contributions

Conceptualisation: JNS. Investigation: ERR, RLS, SS, YT, DV-C, JNS. Writing and figure production: JNS with input from all authors. Supervision and funding acquisition: XLY, GS, JNS.

Materials & Correspondence

AAV expression plasmids are covered by an MTA with OXGENE (UK). Material requests should be addressed to the corresponding authors.

Acknowledgements and Funding

We thank Robert W. Burgess (The Jackson Laboratory) for generating and sharing the $Yars^{E196K}$ mice, Timothy J. Hines for providing $Yars^{E196K}$ genotyping primers, K. Kevin Pfister (University of Virginia) for donating the p-DIC (S81) antibody, and personnel of the Denny Brown Laboratory for assistance with mouse colonies (UCL). This project was funded by a Medical Research Council award MR/S006990/1 (JNS); a Rosetrees Trust grant M806 (JNS, GS); the UCL Neurogenetic Therapies Programme funded by The Sigrid Rausing Trust (JNS, GS); a Human Frontier Science Program Long-Term Fellowship LT000220/2017-L (SS); a National Institutes of Health R35 award GM139627 (XLY); Wellcome Trust awards 107116/Z/15/Z and 223022/Z/21/Z (GS); and a UK Dementia Research Institute Foundation award UKDRI-1005 (GS).

Conflict of Interest Statement

The technology described in this work has been protected in the patent GB2303495.2 (patent applicant, UCL Business Ltd., status pending), in which JNS and GS are named as inventors. The other authors declare no competing interests.

References

1. M. M. Reilly, S. M. Murphy, M. Laura, Charcot-Marie-Tooth disease. *J Peripher Nerv Syst* **16**, 1-14 (2011).
2. M. A. Saporta, M. E. Shy, Inherited peripheral neuropathies. *Neurol Clin* **31**, 597-619 (2013).
3. E. Schorling *et al.*, Cost of illness in Charcot-Marie-Tooth neuropathy: Results from Germany. *Neurology* **92**, e2027-e2037 (2019).
4. M. M. Reilly, Sorting out the inherited neuropathies. *Pract Neurol* **7**, 93-105 (2007).
5. J. Berciano *et al.*, Intermediate Charcot-Marie-Tooth disease: an electrophysiological reappraisal and systematic review. *J Neurol* **264**, 1655-1677 (2017).
6. M. Pipis, A. M. Rossor, M. Laura, M. M. Reilly, Next-generation sequencing in Charcot-Marie-Tooth disease: opportunities and challenges. *Nat Rev Neurol* **15**, 644-656 (2019).
7. A. M. Rossor, J. M. Polke, H. Houlden, M. M. Reilly, Clinical implications of genetic advances in Charcot-Marie-Tooth disease. *Nat Rev Neurol* **9**, 562-571 (2013).
8. N. Wei, Q. Zhang, X. L. Yang, Neurodegenerative Charcot-Marie-Tooth disease as a case study to decipher novel functions of aminoacyl-tRNA synthetases. *J Biol Chem* **294**, 5321-5339 (2019).
9. A. Antonellis *et al.*, Glycyl tRNA synthetase mutations in Charcot-Marie-Tooth disease type 2D and distal spinal muscular atrophy type V. *Am J Hum Genet* **72**, 1293-1299 (2003).
10. A. Jordanova *et al.*, Disrupted function and axonal distribution of mutant tyrosyl-tRNA synthetase in dominant intermediate Charcot-Marie-Tooth neuropathy. *Nat Genet* **38**, 197-202 (2006).
11. P. Latour *et al.*, A major determinant for binding and aminoacylation of $tRNA^{Ala}$ in cytoplasmic Alanyl-tRNA synthetase is mutated in dominant axonal Charcot-Marie-Tooth disease. *Am J Hum Genet* **86**, 77-82 (2010).
12. Y. S. Hyun *et al.*, Rare variants in methionyl- and tyrosyl-tRNA synthetase genes in late-onset autosomal dominant Charcot-Marie-Tooth neuropathy. *Clin Genet* **86**, 592-594 (2014).
13. J. A. Abbott *et al.*, Substrate interaction defects in histidyl-tRNA synthetase linked to dominant axonal peripheral neuropathy. *Hum Mutat* **39**, 415-432 (2018).
14. P. C. Tsai *et al.*, A recurrent WARS mutation is a novel cause of autosomal dominant distal hereditary motor neuropathy. *Brain* **140**, 1252-1266 (2017).
15. J. He *et al.*, Heterozygous seryl-tRNA synthetase 1 variants cause Charcot-Marie-Tooth disease. *Ann Neurol* **93**, 244-256 (2023).
16. S. N. Oprescu, L. B. Griffin, A. A. Beg, A. Antonellis, Predicting the pathogenicity of aminoacyl-tRNA synthetase mutations. *Methods* **113**, 139-151 (2017).
17. H. Zhang, Z. W. Zhou, L. Sun, Aminoacyl-tRNA synthetases in Charcot-Marie-Tooth disease: A gain or a loss? *J Neurochem* **157**, 351-369 (2021).
18. W. W. Motley *et al.*, Charcot-Marie-Tooth-linked mutant GARS is toxic to peripheral neurons independent of wild-type GARS levels. *PLoS Genet* **7**, e1002399 (2011).
19. S. J. Grice *et al.*, Dominant, toxic gain-of-function mutations in *gars* lead to non-cell autonomous neuropathology. *Hum Mol Genet* **24**, 4397-4406 (2015).
20. S. Niehues *et al.*, Impaired protein translation in *Drosophila* models for Charcot-Marie-Tooth neuropathy caused by mutant tRNA synthetases. *Nat Commun* **6**, 7520 (2015).
21. S. J. Grice, J. N. Sleigh, M. Zameel Cader, Plexin-semaphorin signaling modifies neuromuscular defects in a *Drosophila* model of peripheral neuropathy. *Front Mol Neurosci* **11**, 55 (2018).
22. K. H. Morelli *et al.*, Allele-specific RNA interference prevents neuropathy in Charcot-Marie-Tooth disease type 2D mouse models. *J Clin Invest* **129**, 5568-5583 (2019).
23. W. He *et al.*, CMT2D neuropathy is linked to the neomorphic binding activity of glycyl-tRNA synthetase. *Nature* **526**, 710-714 (2015).
24. W. He *et al.*, Dispersed disease-causing neomorphic mutations on a single protein promote the same localized conformational opening. *Proc Natl Acad Sci U S A* **108**, 12307-12312 (2011).
25. M. C. Childers, M. Regnier, M. Bothwell, A. S. T. Smith, Conformational sampling of CMT-2D associated GlyRS mutations. *Brain Multiphys* **3**, 100054 (2022).
26. J. N. Sleigh *et al.*, Trk receptor signaling and sensory neuron fate are perturbed in human neuropathy caused by *Gars* mutations. *Proc Natl Acad Sci U S A* **114**, E3324-E3333 (2017).
27. Z. Mo *et al.*, Aberrant GlyRS-HDAC6 interaction linked to axonal transport deficits in Charcot-Marie-Tooth neuropathy. *Nat Commun* **9**, 1007 (2018).
28. Q. Cui *et al.*, Diverse CMT2 neuropathies are linked to aberrant G3BP interactions in stress granules. *Cell* **186**, 803-820.e25 (2023).
29. E. L. Spaulding *et al.*, The integrated stress response contributes to tRNA synthetase-associated peripheral neuropathy. *Science* **373**, 1156-1161 (2021).
30. A. Zuko *et al.*, tRNA overexpression rescues peripheral neuropathy caused by mutations in tRNA synthetase. *Science* **373**, 1161-1166 (2021).
31. F. P. Thomas *et al.*, Clinical, neurophysiological and morphological study of dominant intermediate Charcot-Marie-Tooth type C neuropathy. *J Neurol* **263**, 467-476 (2016).
32. T. J. Hines *et al.*, Precision mouse models of *Yars*/dominant intermediate Charcot-Marie-Tooth disease type C and *Sptlc1*/hereditary sensory and autonomic neuropathy type 1. *J Anat* **241**, 1169-1185 (2022).
33. M. J. Nowaczyk *et al.*, A novel multisystem disease associated with recessive mutations in the tyrosyl-tRNA synthetase (*YARS*) gene. *Am J Med Genet A* **173**, 126-134 (2017).
34. A. Tracewska-Siemiatkowska *et al.*, An expanded multi-organ disease phenotype associated with mutations in *YARS*. *Genes* **8**, 381 (2017).
35. D. Blocquel *et al.*, Alternative stable conformation capable of protein misinteraction links tRNA synthetase to peripheral neuropathy. *Nucleic Acids Res* **45**, 8091-8104 (2017).
36. S. Bervoets *et al.*, Transcriptional dysregulation by a nucleus-localized aminoacyl-tRNA synthetase associated with Charcot-Marie-Tooth neuropathy. *Nat Commun* **10**, 5045 (2019).
37. B. Ermanoska *et al.*, Tyrosyl-tRNA synthetase has a noncanonical function in actin bundling. *Nat Commun* **14**, 999 (2023).

38. E. Storkebaum *et al.*, Dominant mutations in the tyrosyl-tRNA synthetase gene recapitulate in *Drosophila* features of human Charcot-Marie-Tooth neuropathy. *Proc Natl Acad Sci U S A* **106**, 11782-11787 (2009).
39. C. A. Froelich, E. A. First, Dominant Intermediate Charcot-Marie-Tooth disorder is not due to a catalytic defect in tyrosyl-tRNA synthetase. *Biochemistry* **50**, 7132-7145 (2011).
40. F. Achilli *et al.*, An ENU-induced mutation in mouse glycyl-tRNA synthetase (*GARS*) causes peripheral sensory and motor phenotypes creating a model of Charcot-Marie-Tooth type 2D peripheral neuropathy. *Dis Model Mech* **2**, 359-373 (2009).
41. K. L. Seburn, L. A. Nangle, G. A. Cox, P. Schimmel, R. W. Burgess, An active dominant mutation of glycyl-tRNA synthetase causes neuropathy in a Charcot-Marie-Tooth 2D mouse model. *Neuron* **51**, 715-726 (2006).
42. J. N. Sleigh *et al.*, Boosting peripheral BDNF rescues impaired *in vivo* axonal transport in CMT2D mice. *JCI Insight* 10.1172/jci.insight.157191 (2023).
43. J. N. Sleigh *et al.*, Chondrolectin affects cell survival and neuronal outgrowth in *in vitro* and *in vivo* models of spinal muscular atrophy. *Hum Mol Genet* **23**, 855-869 (2014).
44. J. N. Sleigh *et al.*, Neuropilin 1 sequestration by neuropathogenic mutant glycyl-tRNA synthetase is permissive to vascular homeostasis. *Sci Rep* **7**, 9216 (2017).
45. C. Welinder, L. Ekblad, Coomassie staining as loading control in Western blot analysis. *J Proteome Res* **10**, 1416-1419 (2011).
46. J. N. Sleigh, S. J. West, G. Schiavo, A video protocol for rapid dissection of mouse dorsal root ganglia from defined spinal levels. *BMC Res Notes* **13**, 302 (2020).
47. J. N. Sleigh, S. J. Grice, R. W. Burgess, K. Talbot, M. Z. Cader, Neuromuscular junction maturation defects precede impaired lower motor neuron connectivity in Charcot-Marie-Tooth type 2D mice. *Hum Mol Genet* **23**, 2639-2650 (2014).
48. J. N. Sleigh, R. W. Burgess, T. H. Gillingwater, M. Z. Cader, Morphological analysis of neuromuscular junction development and degeneration in rodent lumbrical muscles. *J Neurosci Methods* **227**, 159-165 (2014).
49. D. Villarroel-Campos, G. Schiavo, J. N. Sleigh, Dissection, *in vivo* imaging and analysis of the mouse epitrochleoanconeus muscle. *J Anat* **241**, 1108-1119 (2022).
50. K. L. Gibbs, B. Kalmar, J. N. Sleigh, L. Greensmith, G. Schiavo, *In vivo* imaging of axonal transport in murine motor and sensory neurons. *J Neurosci Methods* **257**, 26-33 (2016).
51. L. Restani *et al.*, Botulinum neurotoxins A and E undergo retrograde axonal transport in primary motor neurons. *PLoS Pathog* **8**, e1003087 (2012).
52. J. N. Sleigh, A. P. Tosolini, G. Schiavo, *In vivo* imaging of anterograde and retrograde axonal transport in rodent peripheral nerves. *Methods Mol Biol* **2143**, 271-292 (2020).
53. A. P. Tosolini, D. Villarroel-Campos, G. Schiavo, J. N. Sleigh, Expanding the toolkit for *in vivo* imaging of axonal transport. *J Vis Exp* **178**, e63471 (2021).
54. J. N. Sleigh *et al.*, Mice carrying ALS mutant TDP-43, but not mutant FUS, display *in vivo* defects in axonal transport of signaling endosomes. *Cell Rep* **30**, 3655-3662.e3652 (2020).
55. J. Y. Tinevez *et al.*, TrackMate: An open and extensible platform for single-particle tracking. *Methods* **115**, 80-90 (2017).
56. J. N. Sleigh, A. M. Mech, T. Aktar, Y. Zhang, G. Schiavo, Altered sensory neuron development in CMT2D mice is site-specific and linked to increased GlyRS levels. *Front Cell Neurosci* **14**, 232 (2020).
57. J. N. Sleigh, A. M. Mech, G. Schiavo, Developmental demands contribute to early neuromuscular degeneration in CMT2D mice. *Cell Death Dis* **11**, 564 (2020).
58. M. V. Chao, Neurotrophins and their receptors: a convergence point for many signalling pathways. *Nat Rev Neurosci* **4**, 299-309 (2003).
59. M. C. Park *et al.*, Secreted human glycyl-tRNA synthetase implicated in defense against ERK-activated tumorigenesis. *Proc Natl Acad Sci U S A* **109**, E640-647 (2012).
60. P. C. Goughnour *et al.*, Extracellular vesicles derived from macrophages display glycyl-tRNA synthetase 1 and exhibit anti-cancer activity. *J Extracell Vesicles* **10**, e12029 (2020).
61. L. Grube *et al.*, Mining the secretome of C2C12 muscle cells: Data dependent experimental approach to analyze protein secretion using label-free quantification and peptide based analysis. *J Proteome Res* **17**, 879-890 (2018).
62. S. Casas-Tinto, F. N. Lolo, E. Moreno, Active JNK-dependent secretion of *Drosophila* Tyrosyl-tRNA synthetase by loser cells recruits haemocytes during cell competition. *Nat Commun* **6**, 10022 (2015).
63. J. M. Schwenk *et al.*, The Human Plasma Proteome draft of 2017: Building on the Human Plasma PeptideAtlas from mass spectrometry and complementary assays. *J Proteome Res* **16**, 4299-4310 (2017).
64. A. B. Keeler *et al.*, A developmental atlas of somatosensory diversification and maturation in the dorsal root ganglia by single-cell mass cytometry. *Nat Neurosci* **25**, 1543-1558 (2022).
65. K. Bercsenyi *et al.*, Tetanus toxin entry. Nidogens are therapeutic targets for the prevention of tetanus. *Science* **346**, 1118-1123 (2014).
66. A. P. Tosolini *et al.*, BDNF-dependent modulation of axonal transport is selectively impaired in ALS. *Acta Neuropathol Commun* **10**, 121 (2022).
67. Y. Pan, J. Kafaie, F. P. Thomas, Longitudinal 16-year study of dominant intermediate CMT type C neuropathy. *Muscle Nerve* **61**, 111-115 (2020).
68. Q. Cai *et al.*, Snapin-regulated late endosomal transport is critical for efficient autophagy-lysosomal function in neurons. *Neuron* **68**, 73-86 (2010).
69. M. A. Olenick, R. Dominguez, E. L. F. Holzbaur, Dynein activator Hook1 is required for trafficking of BDNF-signaling endosomes in neurons. *J Cell Biol* **218**, 220-233 (2019).
70. S. L. Reck-Peterson, W. B. Redwine, R. D. Vale, A. P. Carter, The cytoplasmic dynein transport machinery and its many cargoes. *Nat Rev Mol Cell Biol* **19**, 382-398 (2018).
71. D. J. Mitchell *et al.*, Trk activation of the ERK1/2 kinase pathway stimulates intermediate chain phosphorylation and recruits cytoplasmic dynein to signaling endosomes for retrograde axonal transport. *J Neurosci* **32**, 15495-15510 (2012).
72. Z. Wang *et al.*, Adeno-associated virus serotype 8 efficiently delivers genes to muscle and heart. *Nat Biotechnol* **23**, 321-328 (2005).
73. B. Wang *et al.*, Construction and analysis of compact muscle-specific promoters for AAV vectors. *Gene Ther* **15**, 1489-1499 (2008).

74. R. Prior, L. Van Helleputte, V. Benoy, L. Van Den Bosch, Defective axonal transport: A common pathological mechanism in inherited and acquired peripheral neuropathies. *Neurobiol Dis* **105**, 300-320 (2017).
75. D. Beijer, A. Sisto, J. Van Lent, J. Baets, V. Timmerman, Defects in Axonal Transport in Inherited Neuropathies. *J Neuromuscul Dis* **6**, 401-419 (2019).
76. J. N. Sleigh, A. M. Rossor, A. D. Fellows, A. P. Tosolini, G. Schiavo, Axonal transport and neurological disease. *Nat Rev Neurol* **15**, 691-703 (2019).
77. V. Benoy *et al.*, HDAC6 is a therapeutic target in mutant *GARS*-induced Charcot-Marie-Tooth disease. *Brain* **141**, 673-687 (2018).
78. A. S. T. Smith *et al.*, HDAC6 inhibition corrects electrophysiological and axonal transport deficits in a human stem cell-based model of Charcot-Marie-Tooth disease (type 2D). *Adv Biol* **6**, e2101308 (2022).
79. F. A. Court, P. J. Brophy, R. R. Ribchester, Remodeling of motor nerve terminals in demyelinating axons of periaxin-null mice. *Glia* **56**, 471-479 (2008).
80. R. H. Baloh *et al.*, Congenital hypomyelinating neuropathy with lethal conduction failure in mice carrying the *Egr2* I268N mutation. *J Neurosci* **29**, 2312-2321 (2009).
81. K. H. Morelli *et al.*, Severity of demyelinating and axonal neuropathy mouse models is modified by genes affecting structure and function of peripheral nodes. *Cell Rep* **18**, 3178-3191 (2017).
82. L. H. Comley *et al.*, Motor unit recovery following Smn restoration in mouse models of spinal muscular atrophy. *Hum Mol Genet* **31**, 3107-3119 (2022).
83. E. M. C. Fisher, D. M. Bannerman, Mouse models of neurodegeneration: Know your question, know your mouse. *Sci Transl Med* **11** (2019).
84. S. E. Cason, E. L. F. Holzbaur, Selective motor activation in organelle transport along axons. *Nat Rev Mol Cell Biol* **23**, 699-714 (2022).
85. K. Deinhardt *et al.*, Rab5 and Rab7 control endocytic sorting along the axonal retrograde transport pathway. *Neuron* **52**, 293-305 (2006).
86. S. E. Cason *et al.*, Sequential dynein effectors regulate axonal autophagosome motility in a maturation-dependent pathway. *J Cell Biol* **220** (2021).
87. A. R. Santos, D. Comprido, C. B. Duarte, Regulation of local translation at the synapse by BDNF. *Prog Neurobiol* **92**, 505-516 (2010).
88. J. M. Villarin, E. P. McCurdy, J. C. Martinez, U. Hengst, Local synthesis of dynein cofactors matches retrograde transport to acutely changing demands. *Nat Commun* **7**, 13865 (2016).
89. B. Ermanoska *et al.*, CMT-associated mutations in glycyl- and tyrosyl-tRNA synthetases exhibit similar pattern of toxicity and share common genetic modifiers in *Drosophila*. *Neurobiol Dis* **68**, 180-189 (2014).
90. L. Sun *et al.*, CMT2N-causing aminoacylation domain mutants enable Nrp1 interaction with AlaRS. *Proc Natl Acad Sci U S A* **118** (2021).
91. D. Blocquel *et al.*, CMT disease severity correlates with mutation-induced open conformation of histidyl-tRNA synthetase, not aminoacylation loss, in patient cells. *Proc Natl Acad Sci U S A* **116**, 19440-19448 (2019).
92. K. L. Gibbs, L. Greensmith, G. Schiavo, Regulation of Axonal Transport by Protein Kinases. *Trends Biochem Sci* **40**, 597-610 (2015).
93. W. Guo, K. Stoklund Dittlau, L. Van Den Bosch, Axonal transport defects and neurodegeneration: Molecular mechanisms and therapeutic implications. *Semin Cell Dev Biol* **99**, 133-150 (2020).
94. B. Ozes *et al.*, AAV1.NT-3 gene therapy in a CMT2D model: phenotypic improvements in *Gars*$^{P278KY/+}$ mice. *Brain Commun* **3**, fcab252 (2021).

Boosting BDNF in muscle rescues impaired *in vivo* axonal transport in a mouse model of DI-CMTC peripheral neuropathy

Authors: Elena R. Rhymes[1,*], Rebecca L. Simkin[1,*], Sunaina Surana[1,2], Yao Tong[3], David Villarroel-Campos[1], Xiang-Lei Yang[3], Giampietro Schiavo[1,2], James N. Sleigh[1,2,#]

[*] Equal contribution

[#] Corresponding author: James N. Sleigh

Email: j.sleigh@ucl.ac.uk

Supplementary Information

Supplementary Figures S1 – S10

Supplementary Tables S1 – S3

Supplementary References 1 – 4

Supplementary Figures

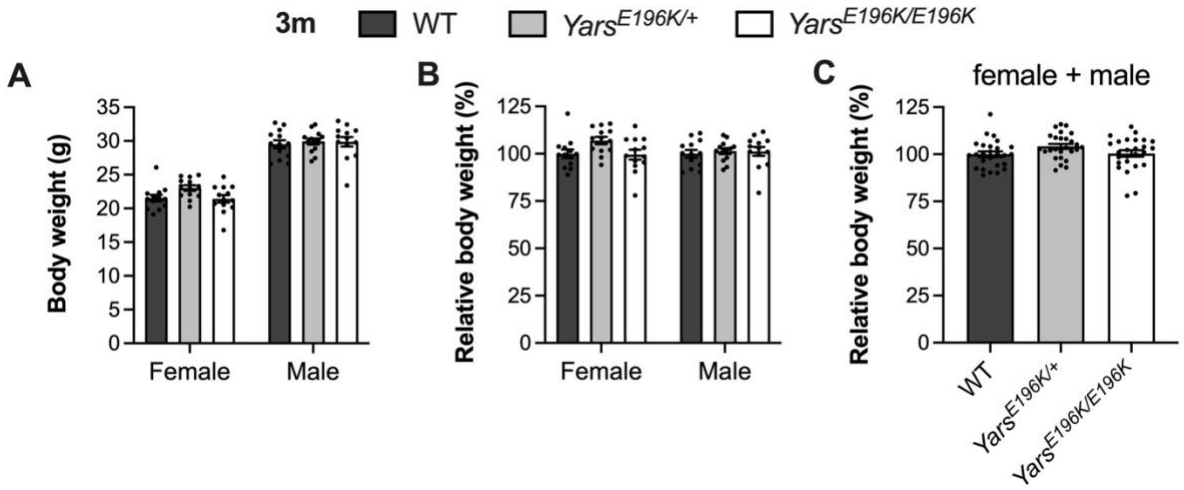

Supplementary Figure S1. *Yars*^{E196K} females and males display normal body weight at 3 months. (**A-B**) There is no difference in body weight (A, genotype $P = 0.169$, sex $P < 0.001$, interaction $P = 0.337$ two-way ANOVA) or relative body weight (B, genotype $P = 0.105$, sex $P = 0.457$, interaction $P = 0.208$ two-way ANOVA) between female or male wild-type, *Yars*$^{E196K/+}$ and *Yars*$^{E196K/E196K}$ mice at 3 months. $n = 13$. (**C**) When relative body weights of females and males are combined, there is still no difference between genotypes ($P = 0.107$ one-way ANOVA). $n = 26$. For all graphs, means ± SEM plotted.

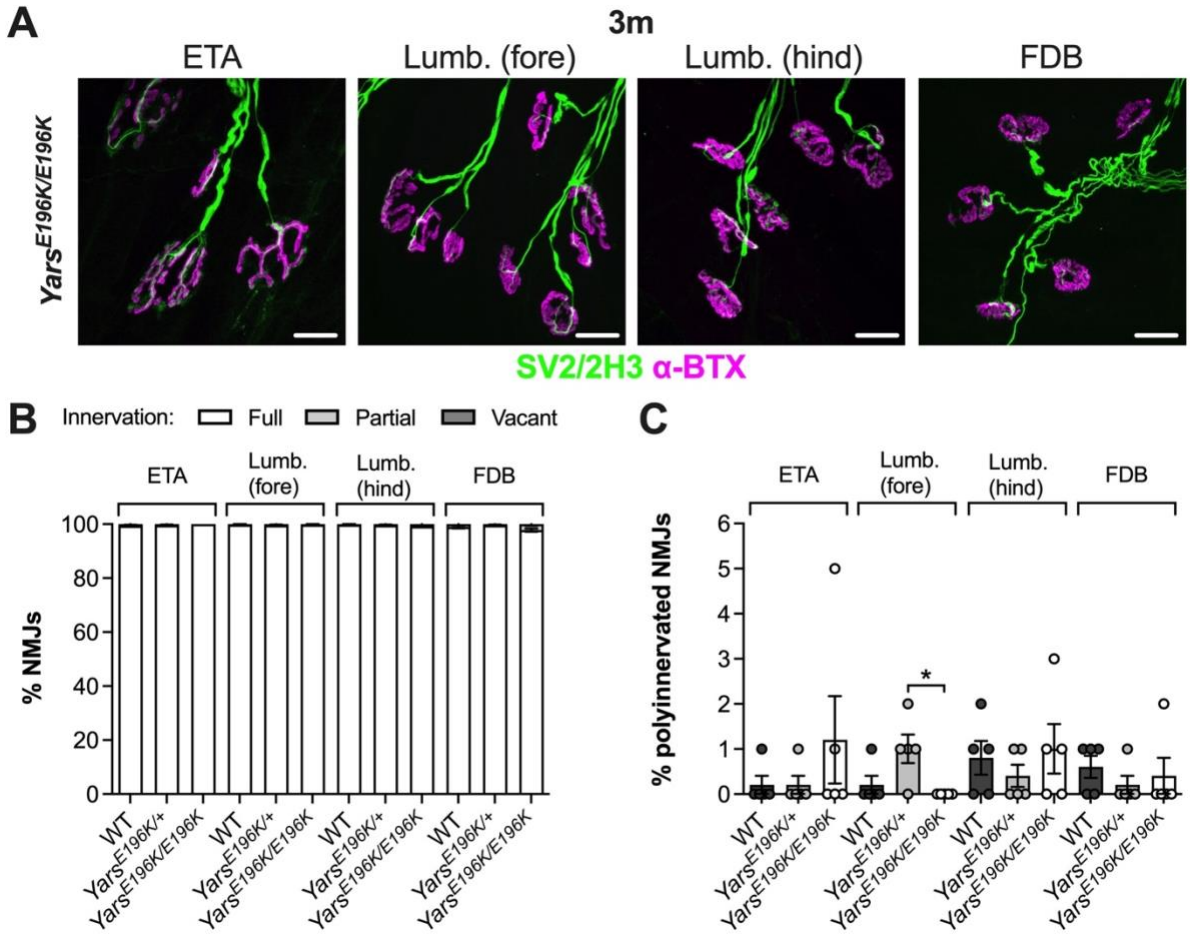

Supplementary Figure S2. Neuromuscular junction innervation and maturation are unaffected in *Yars*^{E196K} mice at 3 months. (**A**) Representative collapsed z-stack confocal images of NMJs in ETA, forepaw lumbrical [*Lumb. (fore)*], hindpaw lumbrical [*Lumb. (hind)*] and FDB muscles in a 3 month-old *Yars*$^{E196K/E196K}$ mouse. Lower motor neurons are visualised using a combination of SV2/2H3 (green) and post-synaptic AChRs with α-BTX (magenta). These images are also representative of wild-type and *Yars*$^{E196K/+}$ mice. Scale bars = 20 µm. (**B**) No difference between genotypes in NMJ innervation was observed in the ETA ($P = 0.251$), the forepaw lumbricals ($P > 0.999$), hindpaw lumbricals ($P = 0.501$) or FDB ($P = 0.063$). (**C**) No meaningful difference between genotypes in the percentage of polyinnervated NMJs was observed in the ETA ($P = 0.725$), the forepaw lumbricals ($P = 0.041$), hindpaw lumbricals (*P*

= 0.750) or FDB (P = 0.501). For all graphs, genotypes were compared using Kruskal-Wallis tests; n = 5; *P < 0.05 Dunn's multiple comparisons test; means ± SEM plotted.

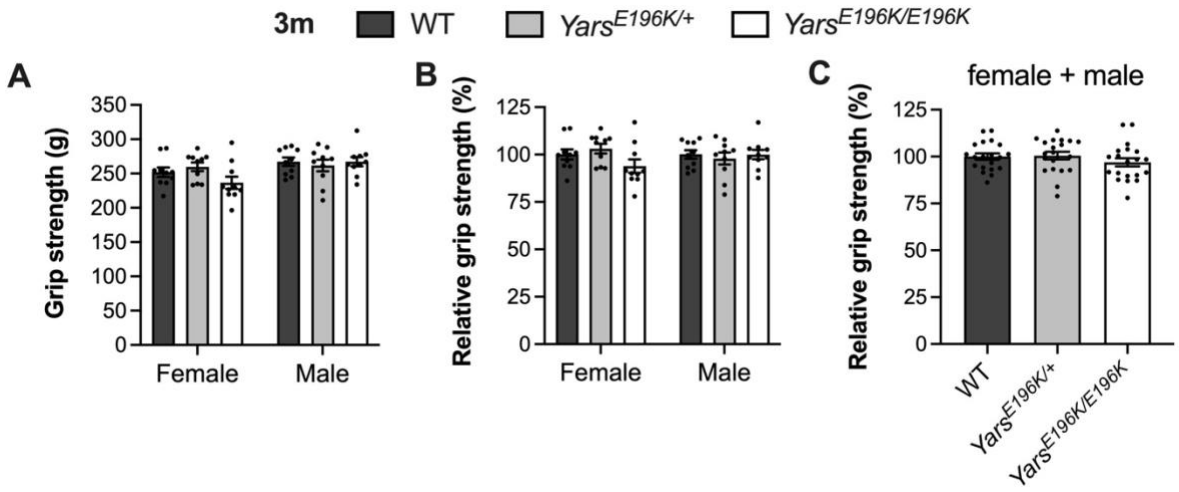

Supplementary Figure S3. Grip strength of *Yars*^{E196K} mice is unaffected at 3 months. (**A-B**) There is no difference in grip strength (A, genotype $P = 0.420$, sex $P < 0.010$, interaction $P = 0.150$ two-way ANOVA) or relative grip strength (B, genotype $P = 0.391$, sex $P = 0.896$, interaction $P = 0.141$ two-way ANOVA) between female or male wild-type, *Yars*$^{E196K/+}$ and *Yars*$^{E196K/E196K}$ mice at 3 months. $n = 10$. (**C**) When relative body weights of females and males are combined, there is still no difference between genotypes ($P = 0.398$ one-way ANOVA). $n = 20$. For all graphs, means ± SEM plotted.

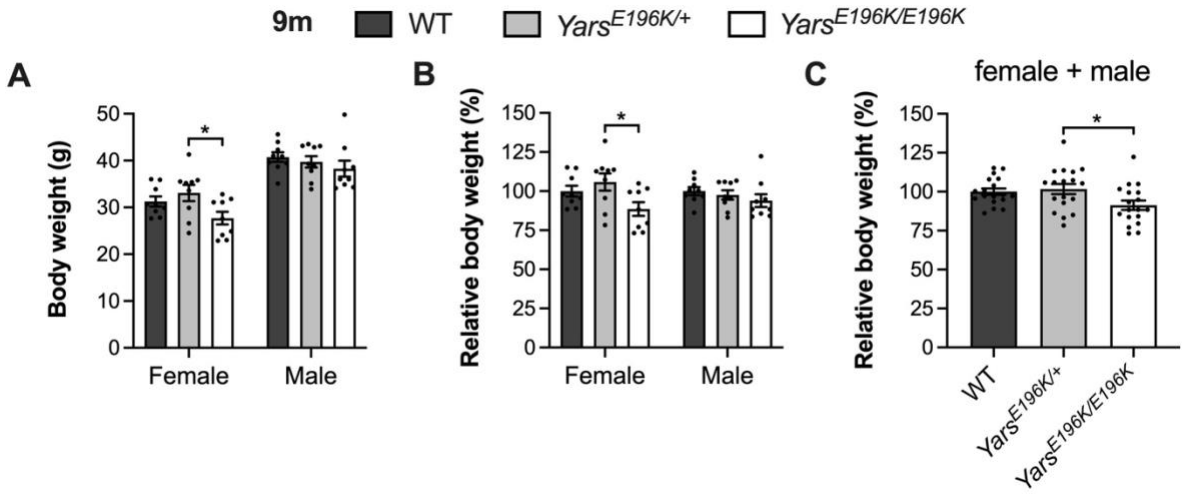

Supplementary Figure S4. Homozygous *Yars*^{E196K} mice display a small reduction in body weight at 9 months. (**A-B**) 9 month-old female *Yars*$^{E196K/E196K}$ mice display a reduction in body weight (A, genotype $P = 0.033$, sex $P < 0.001$, interaction $P = 0.347$ two-way ANOVA) and relative body weight (B, genotype $P = 0.025$, sex $P = 0.764$, interaction $P = 0.230$ two-way ANOVA) compared with *Yars*$^{E196K/+}$. $n = 9$. (**C**) When relative body weights of females and males are combined, *Yars*$^{E196K/E196K}$ mice display a deficit compared to *Yars*$^{E196K/+}$, but not wild-type ($P = 0.025$ one-way ANOVA). $n = 18$. For all graphs, *$P < 0.05$ Šidák's multiple comparisons test; means ± SEM plotted.

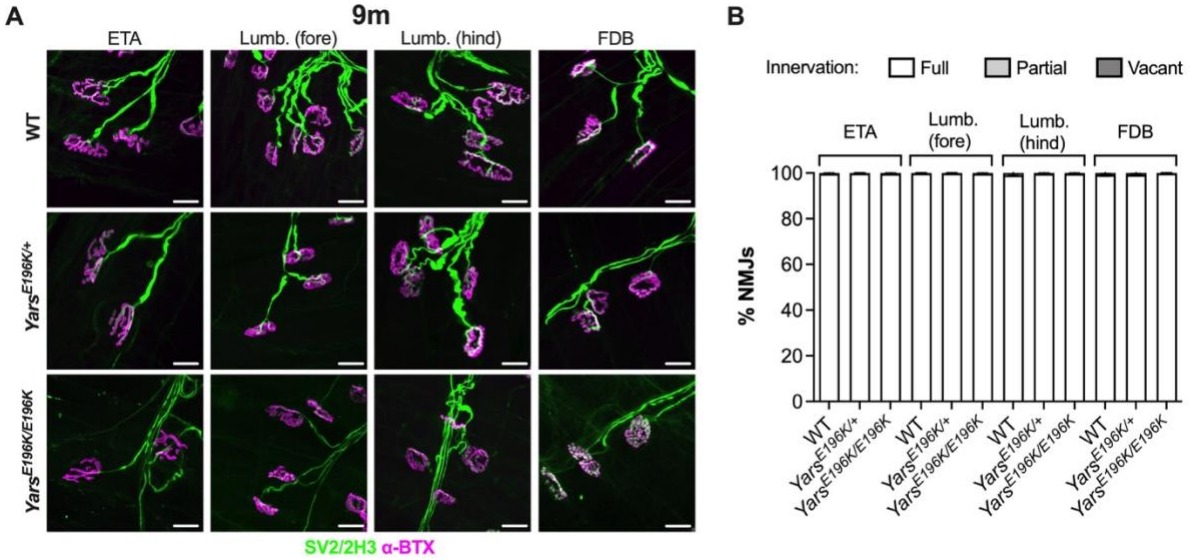

Supplementary Figure S5. Neuromuscular junction innervation remains unaffected in *Yars*^{E196K} mice at 9 months. (**A**) Representative collapsed z-stack confocal images of NMJs in ETA, forepaw lumbrical [*Lumb. (fore)*], hindpaw lumbrical [*Lumb. (hind)*] and FDB muscles in 9 month-old wild-type, *Yars*$^{E196K/+}$ and *Yars*$^{E196K/E196K}$ mice. Lower motor neurons are visualised using a combination of SV2/2H3 (green) and post-synaptic AChRs with α-BTX (magenta). Scale bars = 20 µm. (**B**) No difference between genotypes in NMJ innervation was observed in the ETA ($P > 0.999$), the forepaw lumbricals ($P > 0.999$), hindpaw lumbricals ($P = 0.442$) or FDB ($P = 0.297$). For all graphs, genotypes were compared using Kruskal-Wallis tests; $n = 6$; means ± SEM plotted.

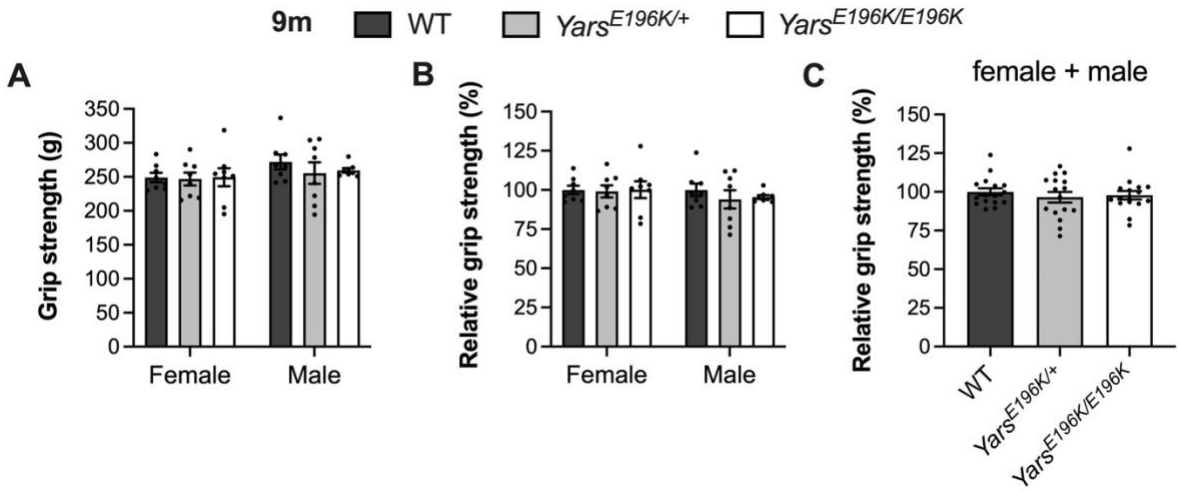

Supplementary Figure S6. Grip strength of *Yars*^{E196K} mice remains unaffected at 9 months. (**A-B**) There is no difference in grip strength (A, genotype P = 0.682, sex P = 0.122, interaction P = 0.773 two-way ANOVA) or relative grip strength (B, genotype P = 0.698, sex P = 0.340, interaction P = 0.792 two-way ANOVA) between female or male wild-type, *Yars*$^{E196K/+}$ and *Yars*$^{E196K/E196K}$ mice at 9 months. n = 8. (**C**) When relative body weights of females and males are combined, there is still no difference between genotypes (P = 0.689 one-way ANOVA). n = 16. For all graphs, means ± SEM plotted.

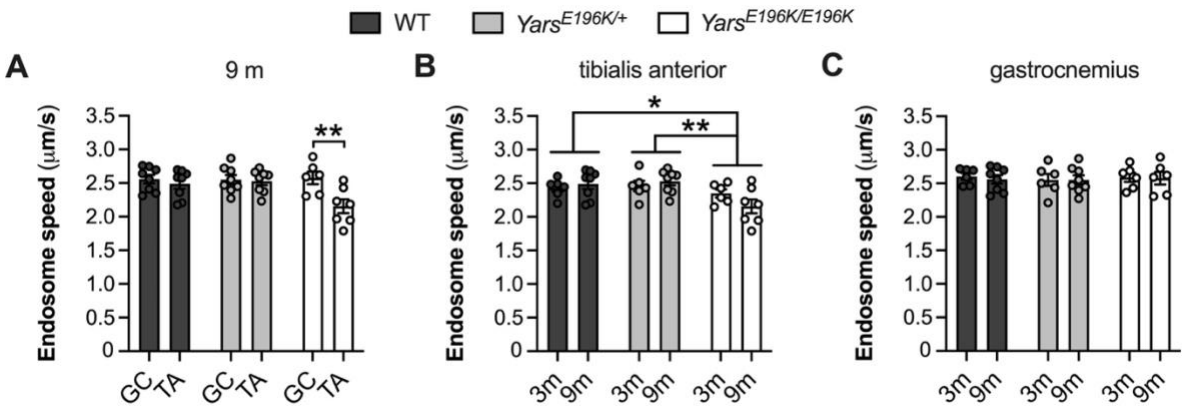

Supplementary Figure S7. 9 month-old *Yars*^{E196K} homozygotes display a selective impairment in *in vivo* axonal transport of signaling endosomes. (**A**) There is a reduction in signaling endosome axonal transport speed in motor axons innervating the tibialis anterior (TA), but not gastrocnemius (GC), in *Yars*$^{E196K/E196K}$ mice aged 9 months. No differences are observed between muscles in wild-type and *Yars*$^{E196K/+}$ mice (genotype $P = 0.068$, muscle $P < 0.010$, interaction $P = 0.033$ two-way ANOVA). (**B-C**) Taking into account endosome transport speeds at 3 (3m) and 9 months (9m) of age, *Yars*$^{E196K/E196K}$ mice display a reduction in the tibialis anterior (genotype $P = 0.007$, age $P = 0.747$, interaction $P = 0.164$ two-way ANOVA), but not gastrocnemius (genotype $P = 0.888$, age $P = 0.752$, interaction $P = 0.953$ two-way ANOVA), compared to wild-type and *Yars*$^{E196K/+}$. For all graphs, $n = 6$-8; *$P < 0.05$, **$P < 0.01$ Šidák's multiple comparisons test; means ± SEM plotted. These data are also presented in **Figure 2** and **Figure 4**.

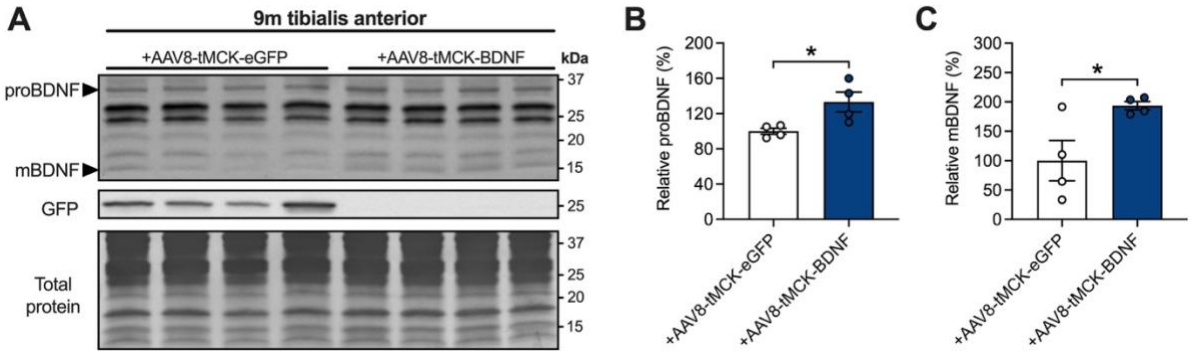

Supplementary Figure S8. AAV8-tMCK drives transgene expression after intramuscular injection. (**A**) Western blots of GFP and BDNF in tibialis anterior muscles from 9 month-old *Yars*$^{E196K/E196K}$ mice that received dual injections of AAV8-tMCK-eGFP versus AAV8-tMCK-BDNF at 8 months. GFP is clearly present in muscles injected with AAV8-tMCK-eGFP. (**B-C**) Densitometric analyses of proBDNF (B) and mature BDNF (mBDNF, C) reveal clear increases in BDNF availability in muscles injected with AAV8-tMCK-BDNF. For all graphs, $n = 4$; $*P < 0.05$ unpaired *t*-test; means ± SEM plotted.

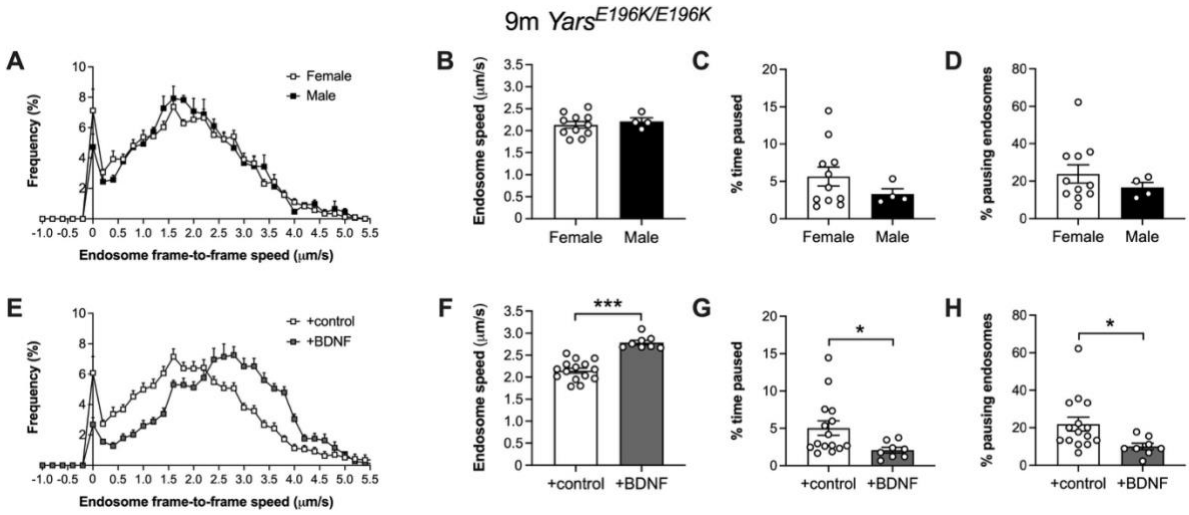

Supplementary Figure S9. Boosting BDNF in muscles of *Yars*^{E196K} homozygotes rescues *in vivo* axonal transport of signaling endosomes. (**A**) Frame-to-frame speed histogram of signalling endosomes being transported within motor neurons innervating the tibialis anterior muscle of 9 month-old *Yars*$^{E196K/E196K}$ females and males. (**B-D**) There is no difference between 9 month-old female and male *Yars*$^{E196K/E196K}$ mice in signaling endosome transport dynamics in tibialis anterior-innervating motor axons. Endosome transport speeds (B, P = 0.579), percentage time paused (C, P = 0.306) and percentage pausing endosomes (D, P = 0.407) all show no difference between sexes. n = 4-11 (**E**) Frame-to-frame speed histogram of signalling endosomes being transported within motor neurons innervating the tibialis anterior muscle of 9 month-old *Yars*$^{E196K/E196K}$ that were either untreated/control-treated (white) or received acute/AAV-mediated treatment with BDNF (grey). (**F-H**) Boosting BDNF in muscle increases signalling endosome transport speed (F, ***P < 0.001), reduces the percentage time paused (G, *P = 0.013) and diminishes the percentage of pausing endosomes (H, *P = 0.033). For all graphs, sexes/treatments were compared using unpaired t-tests; n = 4-11 (A-D) and 8-15 (E-H); means ± SEM plotted. These data are also presented in **Figure 4** and **Figure 6**.

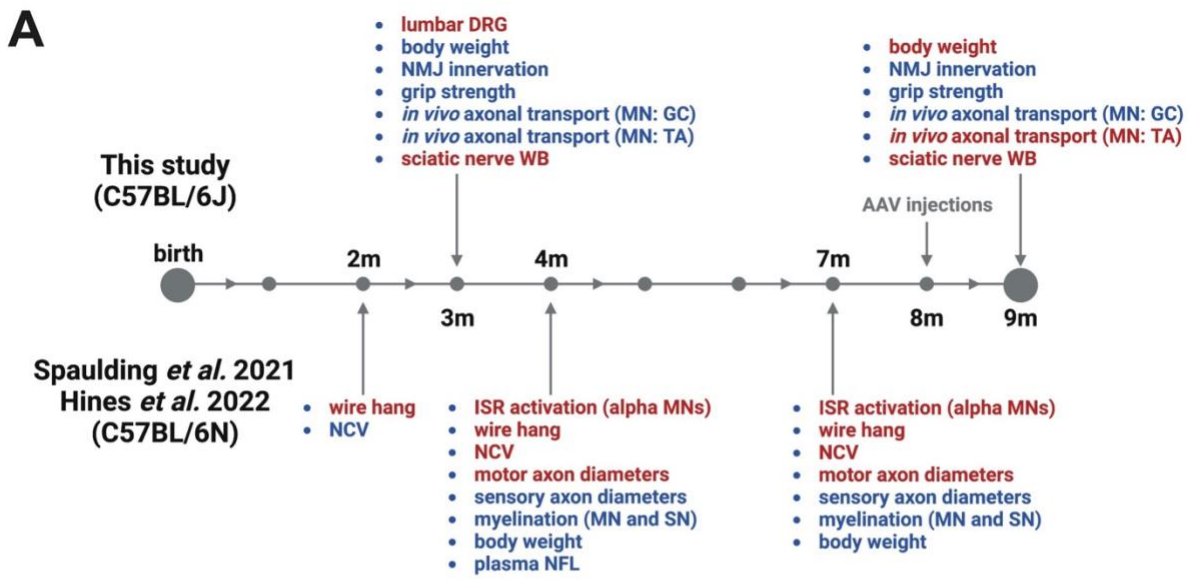

B

Assessment	*Yars* $^{E196K/+}$		*Yars* $^{E196K/E196K}$	
	3m	9m	3m	9m
grip strength				
NMJ innervation				
in vivo axonal transport (MN: GC)				
lumbar DRG				
sciatic nerve WB				
body weight				
in vivo axonal transport (MN: TA)				
in vivo axonal transport (MN: TA) **+BDNF**				
in vivo axonal transport (MN: TA) **+AAV-BDNF**				

Unaffected
Altered/Impaired
Rescued
Not assessed

Supplementary Figure S10. Summary of *Yars*^{E196K} mouse phenotypes. (**A**) Timeline of homozygous *Yars*^{E196K} mouse phenotypes tested and identified in this study (above timeline) and that of Spaulding *et al.* 2021 and Hines *et al.* 2022 (below timeline) (1, 2). Assessments written in blue indicate that no phenotype was observed and those written in red identify a defect (compared to wild-type and/or *Yars*$^{E196K/+}$). Figure created using https://www.biorender.com. (**B**) Summary table of *Yars*^{E196K} mouse phenotypes identified in this study. At 3 months, *Yars*$^{E196K/+}$ mice display perturbed populations of sensory neuron subtypes and altered levels of endosome adaptors in the sciatic nerve, but no deficits in grip strength, NMJ innervation, weight or *in vivo* axonal transport of signaling endosomes. A similar situation is observed at 9 months. *Yars*$^{E196K/E196K}$ mice display a comparable overall phenotype

to *Yars*$^{E196K/+}$ mice, except that at 9 months they also display a selective impairment in *in vivo* axonal transport of signaling endosomes in motor axons innervating the tibialis anterior and not gastrocnemius, as well as a mild, sex-dependent reduction in weight. Boosting BDNF in muscle of *Yars*$^{E196K/E196K}$ mice, either through injection of recombinant BDNF or BDNF-producing AAV, is able to alleviate this transport dysfunction. For both panels, *GC*, gastrocnemius; *ISR*, integrated stress response; *MN*, motor neuron; *NCV*, nerve conduction velocity; *NFL*, Neurofilament light chain; *SN*, sensory neuron; *TA*, tibialis anterior; *WB*, western blot.

Supplementary Tables

Figure	Data	*n*	Sex (WT/Het/Hom)	Age (d)
1B	*in vitro* pull-downs	3	n.a.	n.a.
1D	3 m DRG neuron subtypes	4	2M2F / 2M2F / 3M1F	91-99
S1	3 m body weight	13/26	13M13F / 13M13F / 13M13F	89-99
S2	3 m NMJ phenotypes	5	5M0F / 2M3F / 2M3F	90-99
2B-E	3 m axonal transport in TA	6	5M1F / 6M0F / 3M3F	91-97
2F-I	3 m axonal transport in GC	6	5M1F / 6M0F / 3M3F	91-97
3	3 m sciatic nerve blots	4	4M0F / 2M2F / 2M2F	90-99
S3	3 m grip strength	10/20	10M10F / 10M10F / 10M10F	86-99
S4	9 m body weight	9/18	9M9F / 9M9F / 9M9F	267-285
S5	9 m NMJ phenotypes	6	1M5F / 3M3F / 1M5F	267-280
4A-D	9 m axonal transport in TA	7-8	4M4F / 6M2F / 1M6F	267-279
4E-H	9 m axonal transport in GC	6-8	4M4F / 6M2F / 0M6F	267-279
S6	9 m grip strength	8/16	8M8F / 8M8F / 8M8F	265-287
S7	3 and 9 m axonal transport	6-8	See above	See above
5	9 m sciatic nerve blots	7-8	3M5F / 3M5F / 4M3F	265-280
6A-D	9 m Hom axonal transport +BDNF	4	n.a. / n.a. / 3M1F vs 3M1F	271-272
6E-H	9 m Hom axonal transport +AAV	4	n.a. / n.a. / 0M4F vs 0M4F	273-274
S8	9 m +AAV TA blots	4	n.a. / n.a. / 0M4F vs 0M4F	273-274
S9A-D	9 m Hom axonal transport M vs F	4-11	n.a. / n.a. / 4M vs 11F	267-279
S9E-H	9 m Hom axonal transport +BDNF	8-15	n.a. / n.a. / 4M11F vs 3M5F	267-279

Table S1. Experimental sample sizes and mouse details. *F*, female; *GC*, gastrocnemius; *Het*, *Yars*$^{E196K/+}$; *Hom*, *Yars*$^{E196K/E196K}$; *M*, male; *m*, months; *n*, sample size; *n.a.*, not applicable; *TA*, tibialis anterior; *WT*, wild-type.

Target	Sp.	Clonality	Company /Reference	Catalogue #	RRID	IF dilution	WB dilution
BDNF	Rb	Poly	Novus	NB100-98682	AB_1290643	n/a	1:1,000
DIC	Ms	Mono	Santa Cruz	sc-13524	AB_668849	n/a	1:500
p-DIC (S81)	Rb	Poly	Mitchell *et al.* (3)	n/a	n/a	n/a	1:300
GFP	Rb	Poly	Abcam	ab290	AB_303395	n/a	1:5,000
Hook1	Rb	Mono	Abcam	ab150397	n/a	n/a	1:1,000
Human IgG Fc (HRP)	Gt	Poly	Abcam	ab98624	AB_10673832	n/a	1:10,000
neurofilament (2H3)	Ms	Mono	DSHB	2H3	AB_531793	1:250	n/a
NF200	Ms	Mono	Sigma	N0142	AB_477257	1:500	n/a
peripherin	Rb	Poly	Chemicon	AB1530	AB_90725	1:500	n/a
RILP	Rb	Poly	Abcam	ab140188	n/a	n/a	1:1,000
Snapin	Rb	Poly	Granata *et al.* (4)	n/a	n/a	n/a	1:1,000
SV2 (pan)	Ms	Mono	DSHB	SV2	AB_2315387	1:50	n/a
α-tubulin	Ms	Mono	CST	3873	AB_1904178	n/a	1:2,000
V5	Ms	Mouse	Thermo Fisher	R960-25	AB_2556564	n/a	1:5,000

Table S2. Primary antibodies used in this study. *BDNF*, brain-derived neurotrophic factor; *CST*, Cell Signaling Technology; *DSHB*, Developmental Studies Hybridoma Bank; *DIC*, dynein intermediate chain; *GFP*, green fluorescent protein; *Gt*, goat; *HRP*, horseradish peroxidase; *IF*, immunofluorescence; *Ms*, mouse; *NF*, neurofilament; *Rb*, rabbit; *RILP*, Rab-

interacting lysosomal protein; *RRID*, Research Resource Identifier; *Sp*, species; SV, synaptic vesicle; *WB*, western blotting.

Target	Sp.	Conjugate	Company	Catalogue #	RRID	Dilution
Ms IgG	Dk	AlexaFluor488	Life Technologies	A-21202	AB_141607	1:250-500
Ms IgG	Dk	AlexaFluor555	Life Technologies	A-31570	AB_2536180	1:250-500
Ms IgG	Gt	HRP	Sigma	AP308P	AB_11215796	1:5,000
Rb IgG	Dk	AlexaFluor488	Life Technologies	A-21206	AB_2535792	1:250-500
Rb IgG	Dk	HRP	Bio-Rad	1706515	AB_11125142	1:5,000

Table S3. Secondary antibodies used in this study. *Dk*, donkey; *Gt*, goat; *IgG*, immunoglobulin G; *HRP*, horseradish peroxidase; *Ms*, mouse; *Rb*, rabbit; *RRID*, Research Resource Identifier; *Sp*, species.

Supplementary References

1. E. L. Spaulding *et al.*, The integrated stress response contributes to tRNA synthetase-associated peripheral neuropathy. *Science* **373**, 1156-1161 (2021).
2. T. J. Hines *et al.*, Precision mouse models of *Yars*/dominant intermediate Charcot-Marie-Tooth disease type C and *Sptlc1*/hereditary sensory and autonomic neuropathy type 1. *J Anat* **241**, 1169-1185 (2022).
3. D. J. Mitchell *et al.*, Trk activation of the ERK1/2 kinase pathway stimulates intermediate chain phosphorylation and recruits cytoplasmic dynein to signaling endosomes for retrograde axonal transport. *J Neurosci* **32**, 15495-15510 (2012).
4. A. Granata, R. Watson, L. M. Collinson, G. Schiavo, T. T. Warner, The dystonia-associated protein torsinA modulates synaptic vesicle recycling. *J Biol Chem* **283**, 7568-7579 (2008).